Atmos. Meas. Tech. Discuss., 7, 9603–9671, 2014
www.atmos-meas-tech-discuss.net/7/9603/2014/
doi:10.5194/amtd-7-9603-2014

Atmospheric Measurement Techniques Discussions
Open Access

Probing the sensitivity of polarimetric O_2 A-band measurements to clouds with emphasis on potential OCO-2 and GOSAT retrievals

S. Sanghavi[1,2], **M. Lebsock**[1], **and G. Stephens**[1,2]

[1]Jet Propulsion Laboratory, California Institute of Technology, Pasadena, USA
[2]Colorado State University, Fort Collins, USA

Received: 6 August 2014 – Accepted: 8 September 2014 – Published: 19 September 2014

Correspondence to: S. Sanghavi (suniti.v.sanghavi@jpl.nasa.gov)

Published by Copernicus Publications on behalf of the European Geosciences Union.

Abstract

Clouds play a crucial role in the Earth's radiative budget, yet their climate feedbacks are poorly understood. The advent of space-borne high resolution spectrometers probing the O_2 A-band, such as the GOSAT and OCO-2 satellites, could make it possible to simultaneously retrieve several cloud parameters that play a vital role in the Earth's radiative budget, thereby allowing a reduction of the corresponding uncertainty due to clouds. In this work, the hyperspectral, polarimetric response of the O_2 A-band to mainly three important cloud parameters, viz., optical thickness, top height and droplet size has been studied, revealing a different sensitivity to each for the varying atmospheric absorption strength within the A-band. Cloud optical thickness finds greatest sensitivity in both intensity and polarization measurements at non-absorbing wavelengths. Cloud height had a negligible effect on intensity measurements at non-absorbing wavelengths, but finds maximum sensitivity at an intermediate absorption strength, which increases with cloud height. The same is found to hold for cloud geometric thickness, except that the sensitivity is weaker. Sensitivity to droplet size is generally weaker than to cloud optical thickness to top height at non-absorbing wavelengths and diminishes further with increasing absorption strength. It has been shown that significantly more information on droplet size can be drawn from multiangular measurements. Our results show that, in the absence of sunglint, the backscatter direction is richer in information on droplet size, especially in the glory and rainbow regions. It has been shown that I and Q generally have differing sensitivities to cloud parameters. Thus, accurate measurements of both orthogonal components I_h and I_v (as in GOSAT) are expected to contain more information than measurements of only I, I_h or I_v (as in the case of OCO-2).

AMTD
7, 9603–9671, 2014

1 Introduction

In the context of satellite-based remote sensing, the O_2 A-band has long been regarded a rich source of information on the vertical structure of scattering in the Earth's atmosphere (Fischer and Grassl, 1991; Fischer et al., 1991; O'Brien and Mitchell, 1992; Pfeilsticker et al., 1998; Heidinger and Stephens, 2000; Koelemeijer et al., 2001; Rozanov and Kokhanovsky, 2004; Van Diedenhoven et al., 2007). The O_2 A-band consists of lines of absorption that span a range of optical thickness (measured vertically from top to bottom) covering over 5–6 orders of magnitude in the Earth's atmosphere. Photons of wavelengths coincident with strongly absorbing lines experience rapid extinction and shorter atmospheric path lengths, whereas weaker lines are associated with longer path lengths. Since the O_2 mixing ratio can be assumed constant for remote sensing purposes, it makes absorption due to O_2 at different wavelengths in the A-band a good proxy for the geometric depth within the atmosphere to which most of the incident light could penetrate before being either scattered or (in the case of very strong lines) reaching line saturation.

In addition to the influence of atmospheric absorption, the scattered light is also affected by the properties of the scattering medium. In the case of liquid water clouds, the Stokes vector of the scattered light in an absorbing atmosphere is a function of cloud optical thickness, cloud top height and the size of its constituent droplets (Kokhanovsky, 2006). Cloud microphysics is critical to our understanding of the hydrological cycle (Chahine, 1992; Fowler et al., 1996; Baker, 1997). Droplet size affects cloud brightness (Lohmann and Feichter, 1997; Peng and Lohmann, 2003; Lohmann et al., 2007), thus affecting its ability to reflect back incident solar irradiation. Cloud height also impacts the nature of its radiative feedback (Stephens and Platt, 1987; Slingo and Slingo, 1988; Slingo, 1990; Stephens et al., 2002; Stephens, 2005). The determination of cloud microphysics generally involves the use of thermal infrared and microwave measurements in addition to those in the visible and near infrared ranges (Nakajima and King, 1990; Nakajima et al., 1991; Nakajima and Nakajma, 1995; Platnick and Valero, 1995).

AMTD
7, 9603–9671, 2014

Attempts to determine the height of clouds generally involve strong absorption bands (Kuze and Chance, 1994; Rozanov et al., 2004; Sanghavi et al., 2012) or LIDAR techniques (Dessler et al., 2006; Sassen et al., 2008). The main goal of this work is to examine the cloud information content of the A-band, by taking into consideration not only the intensity but also the polarization of the scattered radiation. The effect of potential multiangular measurements on the determination of cloud droplet size is also probed.

Given that the O_2 A-band is peculiar in that it displays a sensitivity to scattering at different depths of the atmosphere by virtue of several lines of varying absorption strengths, we first examine different factors affecting this sensitivity, such as column absorption strength in Sect. 2 and the microphysics of the scattering cloud in Sect. 3. In Sect. 4, the behavior of the scattered intensity as well as the degree of polarization in response to changes in cloud height (Sect. 4.1), cloud droplet size (Sect. 4.2) and cloud optical thickness (Sect. 4.3) is examined using simulated measurements. In addition to the influence of cloud height, the effect of cloud geometric thickness is also investigated in Sect. 4.1. Also, the gain in information on droplet size using multiangular polarized measurements is studied in Sect. 4.2. Using five distinct wavelengths, corresponding to different column absorption strengths, we examine the behavior of the Stokes vector components I and Q, as well as their linear combinations, $I_v = \frac{1}{2}(I-Q)$ and $I_h = \frac{1}{2}(I+Q)$, within the two-dimensional planes formed by the most important cloud parameters, viz., optical thickness, height and droplet size, in Sect. 4.

The relevance of our findings to observations made by the GOSAT (Hamazaki et al., 2005; Kuze et al., 2009) instrument and the recently launched OCO-2 (Crisp et al., 2004; Pollock et al., 2010) instrument has been pointed out in our concluding remarks in Sect. 6, in view of the fact that both instruments provide hyperspectral measurements of the O_2 A-band, with a spectral resolution of about 0.04 nm. Polarization is included in both instruments, albeit only in the form of $I_v = \frac{1}{2}(I-Q)$ in the case of OCO-2, while GOSAT measures both orthogonal components $I_h = \frac{1}{2}(I+Q)$ and $I_v = \frac{1}{2}(I-Q)$. The ability for multiangle measurements is available to a limited extent in both instruments:

AMTD
7, 9603–9671, 2014

GOSAT provides a range of view angles due to its pointing mechanism which covers ±35° across-track and ±20° along-track, while OCO-2 periodically employs its target mode, during which it is expected to lock its view onto a specific surface location, and retain that view while flying overhead. Over the 9 min time period of a target track pass, OCO-2 can acquire up to 12 960 measurements at local zenith angles that vary between 0° and ±85°, thus providing a good angular coverage over the ground pixel. (Note: in the target mode, OCO-2 measurements are no longer limited to the principal plane, and are thus a linear combination of the Stokes components I, Q and U, where the coefficients for each component are given by a Mueller matrix whose elements depend on the angle between the slit and the principal plane.)

The following section starts with an examination of the dependence of cloud sensitivity on the column absorption strength of the atmosphere.

2 Vertical sensitivity of the O_2 A-band

The absorption cross-section, σ_{abs}, of O_2 at a given wavelength λ varies with height z as a function of pressure and temperature. Using climatological temperature and pressure profiles of a mid-latitude summer and line parameters from the HITRAN 2008 database (Rothman et al., 2009), we obtain total column optical thicknesses in the O_2 A-band as shown in Fig. 1. For the purpose of a sensitivity study, the HITRAN database and a Voigt line-shape are sufficient, but line-mixing effects have to be taken into consideration for retrievals with real data (Tran and Hartmann, 2008). Furthermore, the Rayleigh optical thickness is assumed to be fixed throughout the O_2 A-band at its value at 760 nm.

To determine the sensitivity of the individual lines to the depth of scattering, we assume a laminar plate of Lambertian albedo $\omega_0 = 1$ at a height z above a black surface. The sensitivity, s, to scattering at this plate is proportional to the amount of light

AMTD
7, 9603–9671, 2014

transmitted to the plate (assuming no significant scattering above the surface):

$$s \propto T(z;\mu,\mu_0) = \exp\{-\tau(z)/\overline{\mu}\}, \quad \text{where } \frac{1}{\overline{\mu}} = \frac{1}{\mu_0} + \frac{1}{\mu}, \tag{1}$$

and μ_0 and μ represent the cosines of the solar and view zenith angles. Assuming a constant of proportionality $\frac{1}{\pi}$, we get a sensitivity of

$$s = \frac{1}{\pi} \exp\left\{-\frac{\tau(z)}{\overline{\mu}}\right\}, \tag{2}$$

for the geometry under consideration. Neglecting for simplicity the variation of the absorption cross-section σ_{abs} with height, the exponentially decreasing vertical profile of O_2 allows us to use the following relation for the absorption optical depth of O_2 at an atmospheric level z:

$$\tau_{\text{abs}}(z) = \tau_{\text{abs},0} \exp(-z/H), \tag{3}$$

where $\tau_{\text{abs},0}$ is the total column optical depth of O_2 and $H \approx 8\,\text{km}$ is the scale height. Substituting Eq. (3) in Eq. (2), and expressing the optical depth as a function of wavelength, λ, yields the sensitivity at λ of light reflected at height z in the atmosphere:

$$s(\lambda,z) = \frac{1}{\pi} \exp\left\{-\frac{\tau_{\text{abs},0}(\lambda)}{\overline{\mu}} \exp(-z/H)\right\}. \tag{4}$$

This bivariate sensitivity to z and $\tau_{\text{abs},0}$ is depicted in Fig. 2 for a nadir-viewing geometry with the Sun at zenith ($\mu_0 = \mu = 1$). The top-of-atmosphere (TOA) can be defined as the height above the surface where the molecular concentration becomes negligible (and thus $\tau_{\text{abs}}(\lambda) \to 0$ for all λ). Due to our assumption of Lambertian reflectance, Eq. (2) yields a sensitivity at TOA of $s_{\text{TOA}} = 1/\pi$. It is evident that the non-absorbing

AMTD
7, 9603–9671, 2014

atmosphere is equally sensitive at all heights, since atmospheric scattering has been assumed negligible. (This assumption can be expected to approximate the sensitivity of a Rayleigh scattering atmosphere in the O_2 A-band due to the low optical thickness of Rayleigh scattering in this spectral region: $\tau_{\mathrm{Rayl}}(765\,\mathrm{nm}) = 2.5433 \times 10^{-2}$, Bodhaine et al., 1999.) This changes rapidly with increasing absorption, as the reflected light shows increasingly lower sensitivity to layers closer to the surface. Thus, at $\tau_{\mathrm{abs},0} \approx 40$, there is practically no sensitivity to reflection as high as 30 km above the surface.

By setting a cutoff for the sensitivity s_c, it is possible to estimate the minimum height z_{min} up to which the atmosphere is sensitive to reflection at a given wavelength λ. Setting $s = s_c$ in Eq. (4) and rearranging the terms yields

$$\begin{aligned} z_{\mathrm{min}}(\lambda) &= H\left[\ln\left(\tau_{\mathrm{abs},0}(\lambda)\right) - \ln\left(-\overline{\mu}\ln\left(\pi \cdot s_c\right)\right)\right] \\ &= H\left[\ln\left(\tau_{\mathrm{abs},0}(\lambda)\right) - \ln\left(-\overline{\mu}\ln\left(\frac{s_c}{s_{\mathrm{TOA}}}\right)\right)\right], \end{aligned} \tag{5}$$

since $s_{\mathrm{TOA}} = \frac{1}{\pi}$. The above equation has the linear form $z_{\mathrm{min}}(\lambda) = m \cdot \ln\left(\tau_{\mathrm{abs},0}(\lambda)\right) + c$, where $m = H$ and $c = -H\ln\left(-\overline{\mu}\ln\left(\frac{s_c}{s_{\mathrm{TOA}}}\right)\right)$. This is illustrated by Fig. 3, which shows z_{min} (in red) over the A-band for a cutoff sensitivity of about 10 % of s_{TOA} at $s_c = 0.03$, together with $\tau_{\mathrm{abs},0}$ plotted logarithmically (grey) over the range of the O_2 A-band. The geometry assumed is the same as for Fig. 2, viz., $\mu_0 = \mu = 1$. Negative values of z_{min} indicate that the entire atmospheric column is more sensitive to reflectance than s_c. Equation (6) shows that this occurs when the column absorption falls below the following critical value

$$\tau_{\mathrm{abs},0}(\lambda) \leq -\overline{\mu}\ln\left(\frac{s_c}{s_{\mathrm{TOA}}}\right), \tag{6}$$

Thus, for the geometry $\mu_0 = \mu = 1$, the entire atmospheric column has sensitivity $s > 0.1 \cdot s_{\mathrm{TOA}}$ to reflectance when the column optical thickness is less than a critical value $\tau^c_{\mathrm{abs},0} \approx 1.15$. (For geometries other than the one considered here, $\tau^c_{\mathrm{abs},0} \approx 2.30 \cdot \overline{\mu}$.)

AMTD
7, 9603–9671, 2014

The differential sensitivities to z of lines exceeding $\tau^{c}_{abs,0}$ measureably affect the spectral signature of back-scattered light and thus contribute substantially to the information content of the O_2 A-band on the vertical distribution of scattering species like clouds and aerosol. In the extreme limit, highly absorbing lines such as those at 761.14 nm ($\tau_{abs,0}(761.14\,nm) = 352.607$) and 764.28 nm ($\tau_{abs,0}(764.28\,nm) = 343.588$) are saturated long before the light can penetrate the atmosphere to levels where clouds or aerosols can be expected, rendering them practically useless for the purpose of providing vertical information. Thus, the R-branch of the O_2 A-band (centered roughly around 761 nm), which is much more densely populated by strong absorption lines than the P-branch (centered around $\approx$ 764 nm), exhibits comparatively reduced sensitivity to lower atmospheric scattering heights.

The above discussion assumed a solid laminar reflecting surface at a given atmospheric level. While this served as a good assumption to study the nature of the individual lines constituting the O_2 A-band, it does not suffice to describe backscattering by actual clouds, which are better represented by a vertical distribution (ignoring variations in the two horizontal dimensions) and as a distribution of differently sized droplets. In the following section, we explore the scattering characteristics of a (liquid) cloud as a function of the size of its constituent droplets.

3 Dependence of the scattering properties of clouds on droplet size

Mie theory (van de Hulst, 1957; Deirmendjian, 1969; Wiscombe, 1980; Bohren and Huffman, 1983) allows us to determine the dependence of the single scattering properties of a scattering particle as a function of size. For a particle of size r, the size parameter at wavelength λ is defined as $x = \frac{2\pi r}{\lambda}$. Assuming cloud droplets to be predominantly composed of water (real part of the refractive index, $n_r = 1.33$) with varying degrees of impurity (imaginary part of the refractive index, $n_i = 0, 0.001, 0.005, 0.01, 0.05, 0.1$), Fig. 4 shows the variation of the extinction efficiency, κ, the scattering efficiency, σ, and the single scattering albedo, $\omega_0 = \frac{\sigma}{\kappa}$ with respect to the size parameter x. As expected,

AMTD
7, 9603–9671, 2014

κ approaches the asymptotic value of 2 as $x \to \infty$. Thus, for larger droplets, the extinction cross section is approximately $C_{\text{ext}} = 2\pi r^2$. It is also evident that the single scattering albedo of a given droplet varies only very slightly beyond $x = 50$–100. Thus, for a droplet of size r, the single scattering albedo is practically constant for all wavelengths smaller than $\lambda \approx \frac{2\pi r}{75}$. Generally large-sized cloud droplets lead to a practically constant single scattering albedo throughout the visible range of wavelengths, which, combined with the high order of multiple scattering in clouds causes them to appear white.

We consider pure water clouds ($n = 1.33 - 0.0\imath$) consisting of droplets represented by lognormal size distributions of width $\sigma_0 = 1.13$ around five different median radii $r_0 = 5, 7.5, 10, 12.5$ and 15 nm, as shown in the top panel of Fig. 5. The lognormal distribution is defined in terms of the probability $\rho(r)$ of finding a droplet in the size interval $[r, r + \mathrm{d}r]$ such that

$$\rho(r)\mathrm{d}r = \frac{1}{\sqrt{2\pi}r \ln \sigma_0} \exp\left[-\frac{(\ln r - \ln r_0)^2}{2\ln^2 \sigma_0}\right] \mathrm{d}r. \tag{7}$$

An assumption of a constant cloud optical thickness $\tau = N(r_0)C_{\text{ext}}(r_0)\Delta z$ within the same geometric thickness, Δz, leads to an inverse relation between the number density $N(r_0)$ and the extinction cross section $C_{\text{ext}}(r_0)$ as shown in the bottom panel of Fig. 5. Under the assumption of a pure water cloud, the imaginary part of the refractive index vanishes ($n_{\text{i}} = 0$), resulting in a single scattering albedo $\omega_0 = 1$ for all droplet sizes.

The size of the constituent droplets of a cloud affect its single scattering properties, viz., extinction cross section C_{ext}, single scattering albedo ω_0, and phase matrix $\mathbf{P}(\theta_{\text{scatt}})$, which in turn affect the intensity, polarization and angular distribution of light scattered by the cloud. The choice of a homogenous pure cloud of constant optical and geometric thickness eliminates any size-dependence of the scattered light due to C_{ext} or ω_0. The only property determining the scattering of light as a function of size is thus reduced to the phase matrix $\mathbf{P}(\theta_{\text{scatt}})$.

AMTD
7, 9603–9671, 2014

Figure 6 shows the phase functions $P_v(\theta_{scatt})$ and $P_h(\theta_{scatt})$ governing the scattering of the orthogonal components $I_v = \frac{1}{2}(I - Q)$ and $I_h = \frac{1}{2}(I + Q)$ of the modified Stokes vector, respectively. The features of the phase matrix are most evident in the component of scattered light that has undergone only one scattering event (the single-scatter component). This is true both for the polarization as well as the angular dependence of the scattered light. As the order of scattering increases due to multiple scattering, the radiation field becomes more and more isotropic, thus losing much of the angular form of the original phase matrix.

In the following section, the vertical sensitivity of absorption lines discussed in Sect. 2 as well as the size dependence of the measurement through the phase function of the cloud droplets discussed above are used to closely examine the effects of droplet size, cloud height, cloud optical thickness and cloud geometric thickness on the intensity and polarization of scattered light within the O_2 A-band.

4 Distinguishing cloud parameters using measurements in the O_2 A-band

We use the vector radiative transfer model vSmartMOM (Sanghavi et al., 2014) implementing a corr-*k* approach similar to that of Hasekamp and Butz (2008) using HITRAN 2008 (Rothman et al., 2009) spectral data for modeling O_2 A-band absorption. Climatological vertical profiles of temperature and pressure are adapted from the MODTRAN database (Abreu and Anderson, 1996; Anderson et al., 1986) for the computation of the absorption cross sections. The Stokes vector $\boldsymbol{I} = [I, Q, U, V]$ (scattered radiance normalized with respect to the solar flux) is computed at a spectral resolution of 0.01 nm over the range 759–770 nm for several viewing angles. In the study presented here, only the nadir-viewing geometry has been assumed for all simulations in the following excepting those presented in Sect. 4.2. The Sun is assumed to be at an angle $\theta_0 = 60^\circ$ from the zenith, and the Earth's surface is assumed to be black. The cloud fraction is assumed to be 100 %. Computations of the reflected vector $\boldsymbol{I}$ have been made for cloud optical thickness $\tau_{cloud} = 1.0, 5.0, 10.0$ and 50.0. The cloud geometric thickness

AMTD
7, 9603–9671, 2014

Δz is assumed to be 400 m, within which the cloud is assumed to be uniformly distributed. The cloud top, however, is varied between 2.4 and 12.4 km in intervals of 2 km, i.e., $z_{top} \in \{2.4, 4.4, 6.4, 8.4, 10.4, 12.4\}$ km. The cloud droplets are assumed to be composed of pure water so that their refractive index $n = 1.33 - 0.0i$. The size distributions considered are the same as in Sect. 3, so that they follow Eq. (7) with the median radii $r_0 \in \{5.0, 7.5, 10.0, 12.5, 15.0\}$ µm and a constant width $\sigma_0 = 1.13$. To analyze the reflected intensity I and polarization response $p = |Q|/I$ of the O_2 A-band, we consider a clear-sky atmosphere consisting of only molecular scatterers as shown in Fig. 7, and compare its response with that due to the addition of

1. a cloud of constant optical thickness, $\tau_{cloud} = 10$, geometric thickness, $\Delta z = 400$ m, and size distribution parameter $r_0 = 10$ µm, but varying cloud top heights z_{top} as shown in Fig. 8,
2. a cloud of constant optical thickness, $\tau_{cloud} = 10$, geometric thickness, $\Delta z = 400$ m, and cloud top height $z_{top} = 6.4$ km, but varying cloud median droplet radii r_0 as shown in Fig. 9, and
3. a cloud of constant geometric thickness, $\Delta z = 400$ m, size distribution parameter, $r_0 = 10$ µm, and cloud top height $z_{top} = 6.4$ km, but varying cloud optical thicknesses τ_{cloud} as in Fig. 10.

Figures 7–10, each show the reflected intensity I and the degree of polarization $p = |Q|/I$ (since $U = V = 0$ in a nadir-viewing geometry) in the top and bottom panels, respectively, with each quantity plotted against wavelength on the left and total column absorption on the right. Higher reflected intensities I are indicative of higher isotropicity of the single scattering phase function and/or increased multiple scattering. In contrast, the polarization signal Q is only sensitive to the first few orders of scattering undergone by the incident flux (Schutgens et al., 2004). $Q = I_h - I_v$ becomes increasingly diminished for higher orders of scattering due to the blurring of the differences between the components I_h and I_v. This is because each new scattering event involves a different scattering plane and, consequently, a different rotation of the scattering matrix.

AMTD
7, 9603–9671, 2014

In addition, increased multiple scattering leads to lower values of p due to its inverse relationship with I.

It is evident from Figs. 7–10 that the greatest difference between the pure molecular and cloudy atmospheres is the increase in reflected intensity and the corresponding decrease in the degree of polarization. Both effects are caused mainly by the sharp increase in multiple scattering due to clouds. In the single scattering limit, molecular scattering is more strongly polarizing than cloud droplets at $|\cos\theta_{\text{scatt}}| < 1$ due to the large difference in the Rayleigh phase matrix components P_{h} and P_{v} (see Fig. 6).

As explained in Sect. 2, very strongly absorbing lines already undergo saturation before the incident flux can approach the highest cloud considered here ($z_{\text{top}} = 12.4$ km). Thus, the most of the light scattered at these wavelengths can only have undergone one, and less probably two or more, Rayleigh scattering events before getting detected by the satellite-borne instrument. As a result, both the intensity and the degree of polarization at these wavelengths remain constant irrespective of the cloud scene below. At wavelengths of intermediate strengths of absorption, interaction of light with cloud droplets increases as the light is able to penetrate to greater depths, leading to increasing depolarization caused by increased multiple scattering (as seen also in the purely Rayleigh scattering atmosphere) as well as the relatively depolarizing phase function of clouds. As a result, in the limit of no absorption (at continuum wavelengths), multiple scattering causes the intensity of back-scattered light in cloudy scenes to be much larger than the purely molecular case, whereas the degree of polarization is reduced to levels close to $p = 0$.

4.1 Sensitivity to cloud height

Figure 8 shows the variation of I and p with respect to changes in cloud (top) height, z_{top}, for clouds of constant geometric thickness. It is easy to see that absorbing wavelengths show greater sensitivity to cloud height than non-absorbing or weakly absorbing wavelengths, confirming the conclusions drawn from Figs. 2 and 3 in Sect. 2. As a result, the measured intensity is practically independent of cloud height for

AMTD
7, 9603–9671, 2014

non-absorbing wavelengths. The polarization, however, being sensitive only to the first few orders of scattering, retains its sensitivity to cloud height at non-absorbing wavelengths, since higher clouds reduce the fraction of low-order light scattering due to molecules (Rayleigh scattering) which are more strongly polarizing.

Higher clouds cause more previously unscattered light to be intercepted by cloud droplets, thus also preventing it from penetrating deeper into the atmosphere where it can undergo more absorption due to the higher concentration of O_2 molecules. As a result, the absorption lines are shallower at higher cloud top heights. For lower clouds, the first orders of scattering are dominated to a greater degree by molecular (Rayleigh) scattering, as a result of which Q is larger. Differences in both intensity and polarization are strongest for lines of intermediate absorption strength, as is clearly evident from the right hand side panels of Fig. 8. Stronger lines show more sensitivity to higher clouds, but have reduced sensitivity to lower clouds due to strong extinction. Weaker lines are less capable of distinguishing high clouds but show increased sensitivity to lower clouds. This is evident from the successive shift to the right corresponding to increasing cloud top height of both intensity and polarization with respect to total column absorption in Fig. 8.

Sensitivity to cloud thickness as a function of cloud height

Having seen the effect of moving the same cloud up or down the atmosphere, it is also interesting to investigate the influence of a cloud to changes in its geometric thickness at a given height. To this end, clouds of optical thickness $\tau_{\text{cloud}} = 1$ and $\tau_{\text{cloud}} = 10$, and median droplet radius $r_0 = 5\,\mu\text{m}$ have been considered, each at three different top heights, viz., $z_{\text{top}} = 2.4\,\text{km}$ (Figs. 11 and 12), $z_{\text{top}} = 6.4\,\text{km}$ (Figs. 13 and 14), and $z_{\text{top}} = 12.4\,\text{km}$ (Figs. 15 and 16). An animation covering all heights z_{top} as in the previous section has been included in the accompanying supplementary material. The influence of cloud thickness on the measured intensity I and degree of polarization p at each of these levels, both for the (optically) thin and thick cloud, is examined by varying

AMTD
7, 9603–9671, 2014

the height of the cloud base, such that the cloud thickness is varied from $\Delta z = 200$ m (green) through $\Delta z = 400$ m (red) to $\Delta z = 600$ m (blue).

In each case, thicker clouds (blue dots) are darker than thinner clouds (green dots), for the same cloud top height. This is due to greater extinction of the incident light at a lower cloud base height, predominantly due to molecular extinction. As expected, the degree of polarization shows the opposite effect, with larger signals for lower cloud bases (thicker clouds). It is interesting to note that as the cloud height increases, the maximum sensitivity to cloud thickness, Δz, occurs at increasingly stronger absorption strengths. This evident from a comparison of Figs. 11, 13 and 15 or of Figs. 12, 14 and 16. This is to be expected, since weak lines of absorption are more sensitive to lower atmospheric layers, and vice versa. The sensitivity to Δz also varies with the optical thickness of the cloud: it is greater for $\tau_{\text{cloud}} = 10$ than for $\tau_{\text{cloud}} = 1$.

Figure 17 shows the intensity response of changing the cloud thickness from 200 m to 600 m with respect to cloud top height for different total column absorption strengths for, both, a thick (solid lines) and a thin cloud (broken lines). The non-absorbing wavelength is equally sensitive to all scattering heights in the atmosphere and hence shows no sensitivity to changes in cloud thickness. High absorption strengths, on the other hand, are seen to be sensitive to only high clouds. However, for moderate absorption strengths where $\tau_{\text{abs},0} \lesssim 5$, the sensitivity to cloud geometric thickness is seen to attain a maximum at an intermediate cloud height, which increases with increasing absorption strength. The sensitivity to Δz varies with cloud height on two accounts:

1. Low clouds see the largest gradient of the airmass profile, leading to larger changes with height in the amount of both Rayleigh scattering as well as O_2 absorption. This contributes to the sensitivity to cloud geometric thickness Δz, as also shown by Heidinger and Stephens (2000). However,

2. light reflected back by low clouds undergoes more intermediate extinction by overlying atmospheric layers, than that coming from higher clouds.

AMTD
7, 9603–9671, 2014

These two opposing effects cause a maximum sensitivity at moderate absorption strengths for clouds that are neither too low nor too high, so that lines of absorption strength $\tau_{abs,0} \approx 1$, for example, show maximum sensitivity to cloud thickness for clouds near 6 km.

4.2 Sensitivity to cloud droplet size

For non-absorbing wavelengths (and the geometry considered here), the dependence on r_0 is limited to the increase in isotropicity (and hence a larger multiple scattering component) with decreasing droplet size. This becomes clear by comparing the spectral response of I and p in Fig. 9, where the sensitivity to different r_0 increases with decreasing absorption. The degree of polarization, p, can be seen to be sensitive to r_0 for a larger range of absorption strengths than I, owing to p being boosted by the sensitivity of Q to lower scattering orders concurrent with low I at high $\tau_{abs,0}$. Comparison of Figs. 8 and 9 makes it evident that the O_2 A-band shows greater sensitivity to the cloud top height z than to the size of the cloud droplets r_0 at intermediate strengths of absorption $\tau_{abs,0}$. However, due to the predominance of single scattering within absorbing lines ($\tau_{abs,0} > 0$), these wavelengths can be expected to show greater sensitivity to the angular details of the phase function and hence to the microphysical parameter r_0 as explained in Sect. 3.

This information could be potentially tapped by using multi-angle, polarization-sensitive, hyperspectral measurements which would combine the multiangle, spectropolarimetric capabilities of instruments like POLDER (Deschamps et al., 1994), RSP (Cairns et al., 1999), APS (Peralta et al., 2007), MSPI (Diner et al., 2008), and the future instrument 3MI (Manolis et al., 2013) with hyperspectral capabilities over the O_2 A-band as in SCIAMACHY (Bovensmann et al., 1999), OMI (Levelt et al., 2006), GOSAT (Hamazaki et al., 2005; Kuze et al., 2009) and the recently launched OCO-2 (Crisp et al., 2004; Pollock et al., 2010). As also noted by Boesche et al. (2009) and Frankenberg et al. (2012), a realistic use for the above sensitivity to the microphysical parameter r_0 of p and I through the single scattering phase matrix would be

AMTD
7, 9603–9671, 2014

an application to the target mode of the OCO-2 instrument. While the instrument slit remains perpendicular to the principal plane during OCO-2 Nadir and Glint Mode observations resulting in measurements of $\frac{1}{2}(I-Q)$ over the O_2 A-band, Target mode observations depart from the principal plane, resulting in measurements of a linear combination of the Stokes components $\frac{1}{2}(I+\cos 2\phi_{pp}Q+\sin 2\phi_{pp}U)$ that depends on the angle ϕ_{pp} made by the slit with the principal plane. As mentioned in Sect. 1, the more limited multiangular ability of GOSAT could also be potentially combined with its more comprehensive polarimetric coverage (measuring both $\frac{1}{2}(I-Q)$ and $\frac{1}{2}(I+Q)$) to obtain information on cloud droplet size.

The sensitivity of a multiangular sampling of I and Q to the size-dependent phase function of cloud droplets is examined in more detail in the following section.

Angular dependence of the droplet size sensitivity of the O_2 A-band

In order to examine the angular dependence of the sensitivity of the O_2 A-band to droplet size, we simulate the Stokes components I and Q within the principle plane containing the Sun at a fixed zenith angle of $\theta_0 = 60^\circ$ and 9 view zenith angles $\theta_{view} \in \{-70.5^\circ, -60^\circ, -45.6^\circ, -26.1^\circ, 0^\circ, 26.1^\circ, 45.6^\circ, 60^\circ, 70.5^\circ\}$ as in the MISR instrument (Diner et al., 1998). Using 5 individual wavelengths (see Table 1) within the A-band to represent total column absorption optical thickness near $\tau_{abs,0} = 0, 1, 10, 20$ and 30, simulations of I and Q are made at all 9 view angles for an optically thin ($\tau_{cloud} = 1$) as well as thick ($\tau_{cloud} = 10$) cloud. The thin cloud I and Q simulations are shown in Figs. 19 and 20, respectively, while the corresponding simulations for the optically thick case are respectively shown in Figs. 21 and 22. In each case, three panels show (from left to right) three different cloud heights, viz. $z_{top} = 2.4$, 6.4 and 12.4 km, respectively. In each case, the different absorption strengths are differentiated using the color red for $\tau_{abs,0} = 0$, green for $\tau_{abs,0} = 1$, blue for $\tau_{abs,0} = 10$, magenta for $\tau_{abs,0} = 20$ and black for $\tau_{abs,0} = 30$. The median radius of the cloud, r_0 is represented using different marker shapes, viz., square for $r_0 = 5\,\mu m$, triangle pointing up red for $r_0 = 7.5\,\mu m$, circle for $r_0 = 10\,\mu m$, triangle pointing down for $r_0 = 12.5\,\mu m$, and diamond for $r_0 = 15\,\mu m$.

AMTD
7, 9603–9671, 2014

Due to the assumption of a common cloud optical thickness in both the thin and thick cloud cases, the signals I and Q each depend on the size r_0 only through the scattering matrix $\mathbf{F}(\theta_{\text{scatt}})$, where the scattering angle θ_{scatt} is related to the view angle θ_{view} as

$$\theta_{\text{scatt}} = \cos^{-1}\{\sin\theta_0 \sin|\theta_{\text{view}}|\cos(\phi_{\text{view}} - \phi_0) - \cos\theta_0 \cos|\theta_{\text{view}}|\}. \quad (8)$$

In the above equation, the solar zenith angle is measured such that $0^\circ \le \theta_0 < 90^\circ$. $\phi_0 = 0^\circ$ and ϕ_{view} are the solar and view azimuth angles respectively. View angles at which the Sun is behind the detector are denoted by $\theta_{\text{view}} < 0$ (with $\phi_{\text{view}} = 180^\circ$ in the principal plane), otherwise $\theta_{\text{view}} \ge 0$ (with $\phi_{\text{view}} = 0^\circ$ in the principal plane).

Due to the single scatter relation $\boldsymbol{I} = \mathbf{F} \cdot \boldsymbol{I}_0$, where $\boldsymbol{I} = [I, Q, U, V]^{\mathrm{T}}$ and $\boldsymbol{I}_0$ and $\boldsymbol{I}$ denote the incident and scattered Stokes vectors, the angular distribution of I is governed by the element F_{11} of the scattering matrix, while that of Q (in a frame of reference attached to the scattering plane) is largely driven by the element F_{21}. F_{11} and F_{21} are related to P_{h} and P_{v} of Fig. 6 such that $F_{11} = F_{22} = \frac{1}{2}(P_{\text{h}} + P_{\text{v}})$ while $F_{12} = F_{21} = \frac{1}{2}(P_{\text{h}} - P_{\text{v}})$.

As a result of the above dependencies, the angular nature of the size-dependence of the measured I and Q, respectively, can be expected to be related to the form of F_{11} and F_{21} corresponding to the view angles θ_{view}, as shown in Fig. 18.

Angular sensitivity of I to droplet size r_0

It is evident from the red and green points representing non- and weakly absorbing wavelengths in both Figs. 19 and 21 that the forward scatter directions ($\theta_{\text{view}} > 0$) show higher intensities than backscatter directions ($\theta_{\text{view}} < 0$). This is due to the highly asymmetric nature of the cloud phase function which strongly favors scattering in the forward hemisphere (see Fig. 18, left panel), and the consequently increased multiple scattering observed at scattering angles smaller than 90°. For high absorption, the incident light becomes extinct before reaching the cloud, causing Rayleigh scattering due to atmospheric molecules to dominate the signal. As a result,

AMTD
7, 9603–9671, 2014

these wavelengths (see blue, magenta and black points in Figs. 19 and 21) show increasingly isotropic behavior.

The nadir view angle, $\theta_{view} = 0^{\circ}$, corresponds in the geometry considered here to a scattering angle $\theta_{scatt} = 120^{\circ}$, at which both P_h and P_v in Fig. 6 as well as F_{11} in Fig. 18 can be seen to have diminished sensitivity to droplet size. This sensitivity, however, increases away from $\theta_{scatt} = 120^{\circ}$ in both directions for F_{11}, which drives the angular distribution of the total intensity I. This is reflected in the behaviour of I in the vicinity of the nadir view angle for the low cloud optical thickness case in both directions (both $\theta_{view} \lesssim 0$ and $\theta_{view} \gtrsim 0$) as well as for $\theta_{view} \lesssim 0$ in the high cloud optical thickness case. At higher $|\theta_{view}|$, however, F_{11} alone cannot explain the angular sensitivity of I to r_0.

For the backscatter angles ($\theta_{view} < 0$), the sensitivity to r_0 of the scattered intensities closely resembles the size-dependence of the phase function, revealing a largely low-order scattering signal. As a result, this angular range is well-suited to the detection of droplet size.

At larger forward scatter angles ($\theta_{view} \gg 0$), however, the size-dependence of the intensity either diminishes with increasing θ_{view} as in the case of the thin cloud, or becomes reversed (diamonds at the top, squares at the bottom for $\theta_{view} = 60^{\circ}$ and $\theta_{view} = 70.6^{\circ}$) in the thick cloud case. The high order of multiple scattering within the forward peak causes the original size-dependence of the scattered signal to be blurred. Smaller droplets (e.g., the smallest $r_0 = 5\,\mu m$ represented by squares) show a more isotropic distribution of light than larger ones (e.g., the largest $r_0 = 15\,\mu m$ represented by diamonds), leading to a greater intensity spread around the forward peak but less concentration within the forward peak for smaller droplets, and vice versa.

This "convolution" due to multiple scattering causes the reversal in the size sensitivity at large positive view angles for the thick cloud case and generally diminished size-sensitivity otherwise: increasing cloud optical thickness gives rise to more multiple scattering, and thus more mixing of the forward peak at $\theta_{scatt} = 0^{\circ}$ (stronger for larger droplets) with surrounding aureoles at $0^{\circ} \lesssim \theta_{scatt} < 90^{\circ}$ (stronger for smaller droplets).

AMTD
7, 9603–9671, 2014

These aureoles are represented by the positive view angles considered in the geometry chosen here. As a result, small droplets dominate the scattered signal in the low order scattering regime due to less mixing between the forward peak and the rest of the angular range, while larger droplets dominate the strongly multiple scattered signal. Intermediate orders of scattering, e.g., at larger positive angles in the thin cloud case, do not show any clear dependence on size.

As expected, more wavelengths are sensitive to the phase function for higher clouds, as can be seen across the three panels of Figs. 19 and 21. Less light can penetrate through the absorbing atmosphere to lower clouds, resulting in an intensity signal increasingly dominated by Rayleigh scattering.

Angular sensitivity of Q to droplet size r_0

Figures 20 and 22 show simulations of Q for the thin and thick clouds, respectively. In each case, non- to low-absorption wavelengths clearly reproduce two peaks expected from the scattering matrix element F_{21} on the right panel of Fig. 18: the first caused by the cloud phase function in the rainbow region near the scattering angle $\theta_{\text{scatt}} = 146.1^{\circ}$ (at $\theta_{\text{view}} = -26.1^{\circ}$) and the second occurring at $\theta_{\text{scatt}} = 93.9^{\circ}$ (at $\theta_{\text{view}} = 26.1^{\circ}$) in close vicinity of the Rayleigh polarization peak at $\theta_{\text{scatt}} = 90^{\circ}$. This can be verified by comparing Fig. 20 with Fig. 22: the Rayleigh peak is found to be stronger in the thin cloud case, while the cloud rainbow peak is found to be stronger for the thick cloud.

As may be anticipated, the peak due to cloud droplets in the rainbow region shows the maximum sensitivity to droplet size, followed only by backscatter angles in the glory region (roughly $140^{\circ} < \theta_{\text{scatt}} < 180^{\circ}$, covering $\theta_{\text{view}} = -45.6^{\circ}$ and $\theta_{\text{view}} = -70.6^{\circ}$ in the geometry considered here), but not coincident with the the exact backscatter direction. Single scattering at the exact backscatter angle ($\theta_{\text{scatt}} = 180^{\circ}$ at $\theta_{\text{view}} = -60^{\circ}$) is entirely unpolarized for both molecules and cloud droplets (see right panel of Fig. 18), thus

AMTD
7, 9603–9671, 2014

leading to a weak signal in Q caused only by the less effective scattering events of order larger than one.

The very low values of F_{21} (see both Fig. 18 and Fig. 6) for all cloud droplet sizes considered here at $\theta_{\text{scatt}} = 120^\circ$, coincident with the nadir view angle, $\theta_{\text{view}} = 0^\circ$, makes the nadir Q-signal insensitive to droplet size for both optically thin and thick clouds at all heights.

Significance for multiangular spectropolarimetric remote sensing of cloud microphysics

It is clear that the backscatter region contains information on droplet size, both in the I and the Q components of the Stokes vector. Most of the information is contained at the exact backscatter angle ($\theta_{\text{scatt}} = 180^\circ$) in the I signal without significant contribution from Q. In the rest of the glory region, however, Q has a significant negative contribution, so that $I_{\text{v}} = \frac{1}{2}(I - Q)$ would be more sensitive to droplet size than I alone or $I_{\text{h}} = \frac{1}{2}(I + Q)$. In the rainbow region ($\theta_{\text{scatt}} = 146.1^\circ$, $\theta_{\text{view}} = -26.1^\circ$), however, Q is a strong contributor to the signal contained in I, so that $I_{\text{h}} = \frac{1}{2}(I + Q)$ would carry maximum information on droplet size, while $I_{\text{v}} = \frac{1}{2}(I - Q)$ would miss most of it.

In our example, where the Sun is assumed to be at a zenith angle $\theta_0 = 60^\circ$, the nadir geometry alone would be a relatively poor source of information on droplet size. Multiangular measurements provide the flexibility to choose geometries that are rich in information over more redundant ones, thus leading to potentially more accurate retrievals.

The forward-scatter part of a multiangle swath is relatively poor in its ability to provide information on the droplet size of clouds, mainly because the predominant source of the measured signal is multiple scattering. This is also expected for brighter, nearly isotropically reflecting surfaces, even though the simulations shown here have been made for a black surface. The only exception would be a specular surface (like a relatively calm

AMTD
7, 9603–9671, 2014

ocean) in the Sun glint region, where the forward peak can be strong enough to retain information on the droplet size (Sanghavi et al., 2013, 2014).

4.3 Sensitivity to cloud optical thickness

Figure 10 showcases the expected result of I increasing and p decreasing with increased scattering by cloud droplets. The cloud optical thickness is increased successively from $\tau_{\text{cloud}} = 1$ through $\tau_{\text{cloud}} = 5$ and 10 to $\tau_{\text{cloud}} = 50$, while the cloud top height ($z_{\text{top}} = 6.4\,\text{km}$), its geometric thickness ($\Delta z = 400\,\text{m}$) and its droplet size ($r_0 = 10\,\mu\text{m}$) are kept constant. At high optical thicknesses, the reflectance due to cloud reaches a plateau close to $I = 1/\pi$ for non-absorbing wavelengths since all the reflected light is nearly isotropically distributed.

Sensitivity to τ_{cloud} of both intensity and polarization is greatest when absorption is negligible, and decreases steadily with increasing $\tau_{\text{abs},0}$ as Rayleigh scattering occurring above the cloud top starts to dominate the scattered signal.

5 Distinguishability of the cloud parameters τ_{cloud}, z_{top} and r_0

The previous section dealt with the sensitivity of intensity and polarization to different cloud parameters, treated individually in cases where all other parameters were held fixed. In a real retrieval problem, however, all parameters comprising the state vector $\boldsymbol{x}$ (Rodgers, 2000) are unknown. In such a situation, the covariances due to different parameters complicate the ability of the retrieval algorithm to distinguish between them. Here, we simply show the dependence of I, Q and $\frac{1}{2}(I \pm Q)$ at five different wavelengths within the A-band representing column absorption strengths near $\tau_{\text{abs},0} = 0, 1, 10, 30,$ and 350, respectively, to pairs of parameters we designate as the main components of our state vector, viz., τ_{cloud}, z_{top} and r_0. The geometry considered is the same nadir view geometry as in the previous section.

AMTD
7, 9603–9671, 2014

5.1 Sensitivity to simultaneous changes in z_{top} and r_0

Figures 23–26, respectively, show the sensitivity of measurements of I, Q, $\frac{1}{2}(I-Q)$ and $\frac{1}{2}(I+Q)$ to simultaneous changes in the parameters z_{top} (x axis) and r_0 (y axis) within their respective ranges considered here, for a cloud of optical thickness $\tau_{cloud} = 10$ and geometric thickness $\Delta z = 400$ m.

For I depicted In Fig. 23, the non-absorbing wavelength (first panel) shows sensitivity mainly to the droplet size r_0, but is practically insensitive to z_{top}. The second panel from the left depicts I at a finite absorption strength $\tau_{abs,0} = 1$, at which it is sensitive to all the cloud top heights considered here (according to Eq. 6, the sensitivity at the surface is 5 % of s_{TOA}). It is evident that I, in this case, is predominantly sensitive to z_{top} and shows less sensitivity to the cloud droplet size r_0. However, the sensitivity to droplet size r_0 can be seen to increase with increasing z_{top}, as also found in Sect. 4.2. In the range $\tau_{abs,0} = 10$–30, represented by the third and fourth panels from the left, I shows sensitivity to only higher clouds, as seen in Sect. 4.1. Again, sensitivity to r_0 is low, but increases with cloud height. For low clouds, most of the incident light is already saturated before it can penetrate to z_{top} and subsequently emerge to TOA. Finally, in the extreme case of $\tau_{abs,0} > 300$, seen in the last panel on the right, there is no sensitivity to the cloud, and the signal is dominated only by scant Rayleigh scattering due to fast extinction of the incident light close to TOA.

Q, as shown in Fig. 24, shows comparable sensitivity to both the cloud droplet size r_0 as well as to z_{top} at the non-absorbing wavelength (first panel on the left). This contrast between I and Q can be traced back to the fact that both single and multiple scattering events contribute to I, whereas Q depends mostly on the first 2–3 orders of scattering. As the cloud top height z_{top} increases, so does the relative strength of lower orders of scattering emerging from it at the TOA, creating a height dependent signal. In the low absorption case $\tau_{abs,0} = 1$ (second panel on the left), Q is sensitive mainly to cloud top height z_{top}. Sensitivity to droplet size is greater for smaller r_0. As the atmospheric absorption increases to $\tau_{abs,0} = 10$–30 (third and fourth panels from

AMTD
7, 9603–9671, 2014

the left), sensitivity becomes limited to increasingly higher clouds, in a similar fashion as for I. Again, extremely high absorption, as seen in the right panel obviously shows no sensitivity to the cloud.

Due to the nearly 10 times greater strength of the I signal compared to Q, $\frac{1}{2}(I \pm Q)$ both are very similar to I at most absorbing wavelengths, as can be seen from Figs. 25 and 26. At the non-absorbing wavelength, however, seen in both figures on the first panel to the left, the component of linear polarization perpendicular to the scattering plane formed between the incident solar flux and the view direction, $I_v = \frac{1}{2}(I - Q)$ can be seen to have more sensitivity to z_{top} than $I_h = \frac{1}{2}(I + Q)$, which in turn is more sensitive than only I.

5.2 Sensitivity to simultaneous changes in τ_{cloud} and r_0

Figures 27–30, respectively, show the sensitivity of measurements of I, Q, $\frac{1}{2}(I - Q)$ and $\frac{1}{2}(I + Q)$ to simultaneous changes in the parameters r_0 (x axis) and τ_{cloud} (y axis) within their respective ranges considered here, for a cloud top height of $z_{top} = 6.4$ km and geometric thickness $\Delta z = 400$ m.

Figures 27 shows that I is much more sensitive to cloud optical thickness τ_{cloud} than to cloud droplet size r_0 at all atmospheric absorption strengths except for the saturated case of $\tau_{abs,0} > 300$ in the last panel to the right. In each of the first four panels to the left, the sensitivity to droplet radius is seen to increase with increasing cloud optical thickness upto a peak value, and then decreases with further increase in τ_{cloud}. However, the peak value of the cloud optical thickness at which maximum sensitivity to cloud droplet radius us achieved increases with increasing atmospheric absorption. Consequently, the nonabsorbing wavelength on the left panel shows more sensitivity to r_0 at a cloud optical thickness of $\tau_{cloud} = 5$ and 10 than at $\tau_{cloud} = 1$ (where the signal due to cloud scattering is comparitively weak) or $\tau_{cloud} = 50$ (where a high degree of multiple scattering blurs the size dependence of the received signal). Proceeding from

AMTD
7, 9603–9671, 2014

the second panel on the left towards the fourth, it can be seen that the maximum size sensitivity starts shifting towards increasingly higher optical thicknesses.

Q, as seen in Fig. 28, shows increased sensitivity to smaller sized particles (owing to differences in the scattering matrix seen in Fig. 6) as well as to lower optical thicknesses (because of less multiple scattering) at the non-absorbing wavelength in the leftmost panel. With increasing atmospheric absorption, Q also becomes sensitive to greater cloud optical thicknesses, while increasingly losing sensitivity to droplet size for thin clouds, as can be seen from panels 2–4 from the left.

Again, the infuence of Q on $\frac{1}{2}(I-Q)$ and $\frac{1}{2}(I+Q)$, as seen in Figs. 29 and 30, respectively, is limited due to its weaker signal. However, on closer inspection, $\frac{1}{2}(I+Q)$ is found to have a greater sensitivity to droplet size than I, which in turn is more sensitive than $\frac{1}{2}(I-Q)$. The reason for these differences are accounted for by differences in $\frac{1}{2}(P_\mathrm{h}+P_\mathrm{v})$ and $\frac{1}{2}(P_\mathrm{h}-P_\mathrm{v})$ (see Fig. 18) as explained in Sect. 4.2.

5.3 Sensitivity to simultaneous changes in τ_{cloud} and z_{top}

Figures 31–34, respectively, represent the sensitivity of measurements of I, Q, $\frac{1}{2}(I-Q)$ and $\frac{1}{2}(I+Q)$ to simultaneous changes in the parameters z_{top} (x axis) and τ_{cloud} (y axis) within their respective ranges considered here, for a median cloud droplet radius of $r_0 = 10\,\mu\mathrm{m}$ and geometric thickness $\Delta z = 400\,\mathrm{m}$.

Again, I at the non-absorbing wavelength shown in the first panel to the left on Fig. 31, shows negligible sensitivity to the cloud top height z_{top} compared to the optical thickness τ_{cloud}. The opposite, however, is found to be true of the weakly absorbing atmosphere ($\tau_{\mathrm{abs},0}$) represented by the second panel from the left, where I is found to be most sensitive to z_{top}, with relatively weak sensitivity to cloud optical thickness only at high cloud top heights. As the absorption strength of the atmosphere increases progressively towards the right panel, the signal only remains sensitive to increasingly higher clouds, so that, again, there is no sensitivity at all at $\tau_{\mathrm{abs},0} > 300$.

AMTD
7, 9603–9671, 2014

The sensitivity to Q for a non-absorbing atmosphere, seen in the left panel of Fig. 32, arises mainly from the strong Rayleigh polarization of the nearly depolarized light reflected back by the cloud. The reflected signal is weakest for the optically thin case of $\tau_{\text{cloud}} = 1$, whereas all cases beyond $\tau_{\text{cloud}} \geq 5$ show comparable opacity, leading to the markedly lower signal in Q (ignoring the sign) evident in the case of $\tau_{\text{cloud}} = 1$. This trend is found to continue at all wavelengths irrespective of absorption strength. Since the lowest cloud allows for the largest amount of Rayleigh scattering above it, the strength of the Q signal (again ignoring the sign) is expected to be maximum at the surface and decreases with increasing cloud top heights z_{top}. This relationship, however, is already reversed for an atmospheric absorption strength, $\tau_{\text{abs},0} = 1$, where greater depths within atmosphere also lead to increased extinction due to absorption, thus weakening the signal with increasing depth (decreasing z_{top}). This trend intensifies with increasing absorption strength, so that Q increasingly loses sensitivity to lower cloud top heights z_{top} as seen in the last three panels to the right.

Again, since I is about an order of magnitude stronger than Q, $\frac{1}{2}(I \pm Q)$ do not show large differences in their behavior compared to I, as can be seen from Figs. 33 and 34.

Thus, the main advantage of measuring both $\frac{1}{2}(I \pm Q)$ (as in GOSAT) compared to only I (as in SCIAMACHY) or $\frac{1}{2}(I - Q)$ (as in OCO-2), is the ability to analyze both I and Q independently, which together contain significantly more information than I alone.

6 Conclusions

In this work, a theoretical basis has been established in Sect. 2 providing an approximate relationship (Eq. 5) between the absorption strength of the atmosphere in the O_2 A-band and the maximum depth in the atmosphere to which the backscattered radiance is sensitive to the presence of a scattering medium. Also, the dependence of cloud optical properties, viz., optical thickness, single scattering albedo and phase matrix, on cloud droplet size has been studied in Sect. 3 to support the subsequent analysis in

AMTD
7, 9603–9671, 2014

Sect. 4 of the sensitivity of intensity and polarization as measured by satellite remote sensing to the cloud optical thickness, cloud top height and geometric thickness, as well as cloud droplet size. The main results of this analysis have been summarized in the following:

1. The cloud optical thickness is seen to have the most robust effect of all cloud parameters at practically all atmospheric absorption strengths up to about $\tau_{abs,0} \approx 15$ for the cloud top heights considered here under the assumption of a black surface. The sensitivity of clouds for a finite atmospheric absorption strength increases with increasing cloud height, which is a direct consequence of Eq. (5) derived in Sect. 2.

2. Cloud height has practically no influence on the intensity of reflected light for a non-absorbing atmosphere in the spectral range of the O_2 A-band. However, the sensitivity starts increasing with increasing absorption strength up to about $\tau_{abs,0} = 5$ (for the cloud heights considered here and under the assumption of a black surface). Between $\tau_{abs,0} \approx 5$ and $\tau_{abs,0} \approx 50$, the sensitivity gets increasingly limited to high clouds. Beyond $\tau_{abs,0} \approx 50$, practically no light penetrating the atmosphere to the level of the highest cloud considered ($z_{top} = 12$ km) can be detected at TOA.

3. The sensitivity to cloud geometric thickness is very similar to that of cloud top height, making it potentially difficult to distinguish one from the other. Non-absorbing wavelengths show no sensitivity to cloud thickness, while those with high absorption strengths are only sensitive to high clouds. For moderate absorption strengths like $\tau_{abs,0} = 1$, the sensitivity to cloud geometric thickness is found to increase with increasing cloud height for low clouds up to a cloud height of about 6 km, beyond which the sensitivity falls. This is due to the increasing gradient of scattering and absorbing airmass at lower altitudes countered by simultaneously increasing extinction due to the increasing optical thickness of the overlying atmosphere.

AMTD
7, 9603–9671, 2014

4. Cloud droplet size most strongly affects the intensity at non-absorbing wavelengths, while the sensitivity to droplet size diminishes completely beyond $\tau_{abs,0} \approx 5$ for a nadir view angle with a solar zenith angle of 60°. Multiangle measurements are found to contribute considerably to the sensitivity to droplet size. The possibility of obtaining multiangle data from both GOSAT and OCO-2 has been explored. Backscatter angles in and around the glory region are found to be especially sensitive to droplet size. The contribution of the Stokes component Q is also significant in this angular range, with the strongest contribution in the rainbow region (made at a scattering angle of 146.1° for the viewing geometry considered here).

5. It is found that the orthogonal components $I_h = \frac{1}{2}(I+Q)$ and $I_v = \frac{1}{2}(I-Q)$ of linearly polarized light, both show a behavior more similar to I than to Q since I is usually about an order of magnitude larger. Q, in contrast to I, is predominantly sensitive to the first few orders of scattering of light. Also, it depends more strongly on the element F_{21} of the scattering matrix **F**, while the angular distribution of I is governed by the element F_{11}. It has thus been shown in Sect. 5 that the response of Q to changes in cloud properties is fundamentally different from that of I, adding to the information contained in polarimetric measurements, as also emphasized by Mishchenko et al. (2007a, b). In this respect, the GOSAT instrument, which provides information on both I and Q (assuming sufficient accuracy) due to its measurement of both I_h and I_v, is capable of providing more information than OCO-2, which measures only the perpendicular component I_v.

The main focus of this work has been to explore the broad state space of cloud parameters, aiming at a mainly qualitative perspective on their effect on hyperspectral polarimetric multiangular measurements within the O_2 A-band. This will be followed by a quantitative information content and noise analysis based on the optimal estimation formalism (Rodgers, 2000), in which we shall explore the effect of covariance between

AMTD
7, 9603–9671, 2014

different parameters, measurement error, and the integration of a priori knowledge with the aid of Jacobian matrices provided by vSmartMOM.

The Supplement related to this article is available online at doi:10.5194/amtd-7-9603-2014-supplement.

Acknowledgements. This work has been supported by the NASA Aerosol-Cloud-Ecosystem (ACE) mission project. The authors would like to thank Chris O'Dell of Colorado State University for information on the angle dependent Stokes vector contribution to OCO-2 Target Mode measurements.

This research was carried out at the Jet Propulsion Laboratory, California Institute of Technology, under contract with NASA.

References

Abreu, L. and Anderson, G.: The MODTRAN 2/3 report and LOWTRAN 7 model, Contract, 19628, 0132, 1996. 9612

Anderson, G. P., Clough, S., Kneizys, F., Chetwynd, J., and Shettle, E. P.: AFGL atmospheric constituent profiles (0.120 km), Tech. rep., DTIC Document, 1986. 9612

Baker, M.: Cloud microphysics and climate, Science, 276, 1072–1078, 1997. 9605

Bodhaine, B. A., Wood, N. B., Dutton, E. G., and Slusser, J. R.: On Rayleigh optical depth calculations, J. Atmos. Ocean. Tech., 16, 1072–1078, 1999. 9609

Boesche, E., Stammes, P., and Bennartz, R.: Aerosol influence on polarization and intensity in near-infrared O_2 and CO_2 absorption bands observed from space, J. Quant. Spectrosc. Ra., 110, 223–239, 2009. 9617

Bohren, C. F. and Huffman, D. R.: Absorption and Scattering of Light by Small Particles, Wiley, New York, 1983. 9610

AMTD
7, 9603–9671, 2014

Bovensmann, H., Burrows, J., Buchwitz, M., Frerick, J., Noël, S., Rozanov, V., Chance, K., and Goede, A.: SCIAMACHY: mission objectives and measurement modes, J. Atmos. Sci., 56, 127–150, 1999. 9617

Cairns, B., Russell, E. E., and Travis, L. D.: Research scanning polarimeter: calibration and ground-based measurements, SPIE's International Symposium on Optical Science, Engineering, and Instrumentation, International Society for Optics and Photonics, 186–196, 1999. 9617

Chahine, M. T.: The hydrological cycle and its influence on climate, Nature, 359, 373–380, 1992. 9605

Crisp, D., Atlas, R. M., Breon, F.-M., Brown, L. R., Burrows, J. P., Ciais, P., Connor, B. J., Doney, S. C., Fung, I. Y., Jacob, D. J., Miller, C. E., O'Brien, D., Pawson, S., Randerson, J. T., Rayner, P., Salawitch, R. J., Sander, S. P., Sen, B., Stephens, G. L., Tans, P. P., Toon, G. C., Wennberg, P. O., Wofsy, S. C., Yung, Y. L., Kuang, Z., Chudasama, B., Sprague, G., Weiss, B., Pollock, R., Kenyon, D., and Schroll, S.: The orbiting carbon observatory (OCO) mission, Adv. Space Res., 34, 700–709, 2004. 9606, 9617

Deirmendjian, D.: Electromagnetic Radiation Scattering by Spherical Polydispersed Particles, Elsevier, New York, 1969. 9610

Deschamps, P.-Y., Bréon, F.-M., Leroy, M., Podaire, A., Bricaud, A., Buriez, J.-C., and Seze, G.: The POLDER mission: instrument characteristics and scientific objectives, IEEE T. Geosci. Remote, 32, 598–615, 1994. 9617

Dessler, A., Palm, S., and Spinhirne, J.: Tropical cloud-top height distributions revealed by the Ice, Cloud, and Land Elevation Satellite (ICESat)/Geoscience Laser Altimeter System (GLAS), J. Geophys. Res.-Atmos., 111, D12215, doi:10.1029/2005JD006705, 2006. 9606

Diner, D. J., Mischna, M., Chipman, R. A., Davis, A. B., Cairns, B., Davies, R., Kahn, R. A., Muller, J.-P., and Torres, O.: Multi-angle Imaging SpectroRadiometer (MISR) instrument description and experiment overview, IEEE T. Geosci. Remote, 36, 1072–1087, 1998. 9618

Diner, D. J., Mischna, M., Chipman, R. A., Davis, A., Cairns, B., Davies, R., Kahn, R. A., Muller, J.-P., and Torres, O.: WindCam and MSPI: two cloud and aerosol instrument concepts derived from Terra/MISR heritage, in: Society of Photo-Optical Instrumentation Engineers (SPIE) Conference Series, 7081, 25 pp., 2008. 9617

Fischer, J. and Grassl, H.: Detection of cloud-top height from backscattered radiances within the oxygen A band. Part 1: Theoretical study, J. Appl. Meteorol., 30, 1245–1259, 1991. 9605

AMTD
7, 9603–9671, 2014

Fischer, J., Cordes, W., Schmitz-Peiffer, A., Renger, W., and Mörl, P.: Detection of cloud-top height from backscattered radiances within the oxygen A band. Part 2: Measurements, J. Appl. Meteorol., 30, 1260–1267, 1991. 9605

Fowler, L. D., Randall, D. A., and Rutledge, S. A.: Liquid and ice cloud microphysics in the CSU general circulation model. Part 1: Model description and simulated microphysical processes, J. Climate, 9, 489–529, 1996. 9605

Frankenberg, C., Hasekamp, O., O'Dell, C., Sanghavi, S., Butz, A., and Worden, J.: Aerosol information content analysis of multi-angle high spectral resolution measurements and its benefit for high accuracy greenhouse gas retrievals, Atmos. Meas. Tech., 5, 1809–1821, doi:10.5194/amt-5-1809-2012, 2012. 9617

Hamazaki, T., Kaneko, Y., Kuze, A., and Kondo, K.: Fourier transform spectrometer for greenhouse gases observing satellite (GOSAT), Fourth International Asia–Pacific Environmental Remote Sensing Symposium 2004: Remote Sensing of the Atmosphere, Ocean, Environment, and Space, International Society for Optics and Photonics, 73–80, 2005. 9606, 9617

Hasekamp, O. P. and Butz, A.: Efficient calculation of intensity and polarization spectra in vertically inhomogeneous scattering and absorbing atmospheres, J. Geophys. Res.-Atmos., 113, 20309, doi:10.1088/0004-637X/743/1/12, 2008. 9612

Heidinger, A. K. and Stephens, G. L.: Molecular line absorption in a scattering atmosphere. Part II: Application to remote sensing in the O_2 A band, J. Atmos. Sci., 57, 1615–1634, 2000. 9605, 9616

Koelemeijer, R. B., Stammes, P., Hovenier, J., and de Haan, J.: A fast method for retrieval of cloud parameters using oxygen A band measurements from the Global Ozone Monitoring Experiment, J. Geophys. Res.-Atmos., 106, 3475–3490, 2001. 9605

Kokhanovsky, A. A.: Cloud Optics, Vol. 34, Springer, 2006. 9605

Kuze, A. and Chance, K. V.: Analysis of cloud top height and cloud coverage from satellites using the O_2 A and B bands, J. Geophys. Res.-Atmos., 99, 14481–14491, 1994. 9606

Kuze, A., Suto, H., Nakajima, M., and Hamazaki, T.: Thermal and near infrared sensor for carbon observation Fourier-transform spectrometer on the Greenhouse Gases Observing Satellite for greenhouse gases monitoring, Appl. Optics, 48, 6716–6733, 2009. 9606, 9617

Levelt, P. F., van den Oord, G. H., Dobber, M. R., Malkki, A., Visser, H., de Vries, J., Stammes, P., Lundell, J. O., and Saari, H.: The Ozone Monitoring Instrument, IEEE T. Geosci. Remote, 44, 1093–1101, 2006. 9617

AMTD
7, 9603–9671, 2014

Lohmann, U. and Feichter, J.: Impact of sulfate aerosols on albedo and lifetime of clouds: a sensitivity study with the ECHAM4 GCM, J. Geophys. Res.-Atmos., 102, 13685–13700, 1997. 9605

Lohmann, U., Stier, P., Hoose, C., Ferrachat, S., Kloster, S., Roeckner, E., and Zhang, J.: Cloud microphysics and aerosol indirect effects in the global climate model ECHAM5-HAM, Atmos. Chem. Phys., 7, 3425–3446, doi:10.5194/acp-7-3425-2007, 2007. 9605

Manolis, I., Grabarnik, S., Caron, J., Bézy, J.-L., Loiselet, M., Betto, M., Barré, H., Mason, G., and Meynart, R.: The MetOp second generation 3MI instrument, SPIE Remote Sensing, 88890J, International Society for Optics and Photonics, 2013. 9617

Mishchenko, M. I., Cairns, B., Hansen, J. E., Travis, L. D., Kopp, G., Schueler, C. F., Fafaul, B. A., Hooker, R. J., Maring, H. B., and Itchkawich, T.: Accurate monitoring of terrestrial aerosols and total solar irradiance: introducing the Glory Mission, B. Am. Meteorol. Soc., 88, 677–691, 2007a. 9629

Mishchenko, M. I., Geogdzhayev, I. V., Cairns, B., Carlson, B. E., Chowdhary, J., Lacis, A. A., Liu, L., Rossow, W. B., and Travis, L. D.: Past, present, and future of global aerosol climatologies derived from satellite observations: a perspective, J. Quant. Spectrosc. Ra., 106, 325–347, 2007b. 9629

Nakajima, T. and King, M. D.: Determination of the optical thickness and effective particle radius of clouds from reflected solar radiation measurements. Part I: Theory, J. Atmos. Sci., 47, 1878–1893, 1990. 9605

Nakajima, T., King, M. D., Spinhirne, J. D., and Radke, L. F.: Determination of the optical thickness and effective particle radius of clouds from reflected solar radiation measurements. Part II: Marine stratocumulus observations, J. Atmos. Sci., 48, 728–751, 1991. 9605

Nakajima, T. Y. and Nakajma, T.: Wide-area determination of cloud microphysical properties from NOAA AVHRR measurements for FIRE and ASTEX regions, J. Atmos. Sci., 52, 4043–4059, 1995. 9605

O'Brien, D. and Mitchell, R.: Error estimates for retrieval of cloud-top pressure using absorption in the A band of oxygen, J. Appl. Meteorol., 31, 1179–1192, 1992. 9605

Peng, Y. and Lohmann, U.: Sensitivity study of the spectral dispersion of the cloud droplet size distribution on the indirect aerosol effect, Geophys. Res. Lett., 30, 1507, doi:10.1029/2003GL017192, 2003. 9605

Peralta, R. J., Nardell, C., Cairns, B., Russell, E. E., Travis, L. D., Mishchenko, M. I., Fafaul, B. A., and Hooker, R. J.: Aerosol polarimetry sensor for the Glory Mission, International Symposium

AMTD
7, 9603–9671, 2014

on Multispectral Image Processing and Pattern Recognition, International Society for Optics and Photonics, 67865L, 2007. 9617

Pfeilsticker, K., Erle, F., Funk, O., Veitel, H., and Platt, U.: First geometrical pathlengths probability density function derivation of the skylight from spectroscopically highly resolving oxygen A-band observations: 1. Measurement technique, atmospheric observations and model calculations, J. Geophys. Res.-Atmos., 103, 11483–11504, 1998. 9605

Platnick, S. and Valero, F. P.: A validation of a satellite cloud retrieval during ASTEX, J. Atmos. Sci., 52, 2985–3001, 1995. 9605

Pollock, R., Haring, R. E., Holden, J. R., Johnson, D. L., Kapitanoff, A., Mohlman, D., Phillips, C., Randall, D., Rechsteiner, D., Rivera, J., Rodriguez, J. I., Schwochert, M. A., and Sutin, B. M.: The Orbiting Carbon Observatory Instrument: performance of the OCO instrument and plans for the OCO-2 instrument, in: Remote Sensing, International Society for Optics and Photonics, 78260W, 2010. 9606, 9617

Rodgers, C. D.: Inverse Methods for Atmospheric Sounding: Theory and Practice, Vol. 2, World Scientific, Singapore, 2000. 9623, 9629

Rothman, L. S., Gordon, I. E., Barbe, A., Benner, D. C., Bernath, P. F., Birk, M., Boudon, V., Brown, L. R., Campargue, A., Champion, J.-P., Chance, K., Coudert, L. H., Dana, V., Devi, V. M., Fally, S., Flaud, J.-M., Gamache, R. R., Goldman, A., Jaquemart, D., Kleiner, I., Lacome, N., Lafferty, W. J., Mandin, J.-Y., Massie, S. T., Mikhailenko, S. N., Miller, C. E., Moazzen-Ahmadi, N., Naumenko, O. V., Nikitin, A. V., Orphal, J., Perevalov, V. I., Perrin, A., Predoi-Cross, A., Rinsland, C. P., Rotger, M., Simeckova, M., Smith, M. A. H., Sung, K., and Tashkun, S. A.: The HITRAN 2008 molecular spectroscopic database, J. Quant. Spectrosc. Ra., 110, 533–572, 2009. 9607, 9612

Rozanov, V. V. and Kokhanovsky, A. A.: Semianalytical cloud retrieval algorithm as applied to the cloud top altitude and the cloud geometrical thickness determination from top-of-atmosphere reflectance measurements in the oxygen A band, J. Geophys. Res.-Atmos., 109, D05202, doi:10.1029/2003JD004104, 2004. 9605

Rozanov, V. V., Kokhanovsky, A. A., and Burrows, J. P.: The determination of cloud altitudes using GOME reflectance spectra: multilayered cloud systems, IEEE T. Geosci. Remote, 42, 1009–1017, 2004. 9606

Sanghavi, S., Martonchik, J. V., Landgraf, J., and Platt, U.: Retrieval of the optical depth and vertical distribution of particulate scatterers in the atmosphere using O_2 A- and B-band

AMTD
7, 9603–9671, 2014

SCIAMACHY observations over Kanpur: a case study, Atmos. Meas. Tech., 5, 1099–1119, doi:10.5194/amt-5-1099-2012, 2012. 9606
Sanghavi, S., Martonchik, J. V., Davis, A. B., and Diner, D. J.: Linearization of a scalar matrix operator method radiative transfer model with respect to aerosol and surface properties, J. Quant. Spectrosc. Ra., 116, 1–16, 2013. 9623
Sanghavi, S., Davis, A. B., and Eldering, A.: vSmartMOM: a vector matrix operator method-based radiative transfer model linearized with respect to aerosol properties, J. Quant. Spectrosc. Ra., 133, 412–433, 2014. 9612, 9623
Sassen, K., Wang, Z., and Liu, D.: Global distribution of cirrus clouds from CloudSat/Cloud-Aerosol Lidar and Infrared Pathfinder Satellite Observations (CALIPSO) measurements, J. Geophys. Res.-Atmos., 113, D00A12, doi:10.1029/2008JD009972, 2008. 9606
Schutgens, N., Tilstra, L., Stammes, P., and Bréon, F.-M.: On the relationship between Stokes parameters *Q* and *U* of atmospheric ultraviolet/visible/near-infrared radiation, J. Geophys. Res.-Atmos., 109, D09205, doi:10.1029/2003JD004081, 2004. 9613
Slingo, A.: Sensitivity of the Earth's radiation budget to changes in low clouds, Nature, 343, 49–51, 1990. 9605
Slingo, A. and Slingo, J.: The response of a general circulation model to cloud longwave radiative forcing. I: Introduction and initial experiments, Q. J. Roy. Meteorol. Soc., 114, 1027–1062, 1988. 9605
Stephens, G. L.: Cloud feedbacks in the climate system: a critical review, J. Climate, 18, 237–273, 2005. 9605
Stephens, G. L. and Platt, C.: Aircraft observations of the radiative and microphysical properties of stratocumulus and cumulus cloud fields, J. Clim. Appl. Meteorol., 26, 1243–1269, 1987. 9605
Stephens, G. L., Vane, D. G., Boain, R. J., Mace, G. G., Sassen, K., Wang, Z., Illingworth, A. J., O'Connor, E. J., Rossow, W. B., Durden, S. L., Miller, S. D., Austin, R. T., Benedetti, A., and Mirescu, C.: The CloudSat mission and the A-Train: a new dimension of space-based observations of clouds and precipitation, B. Am. Meteorol. Soc., 83, 1771–1790, 2002. 9605
Tran, H. and Hartmann, J.-M.: An improved O_2 A band absorption model and its consequences for retrievals of photon paths and surface pressures, J. Geophys. Res.-Atmos., 113, D18104, doi:10.1029/2008JD010011, 2008. 9607
van de Hulst, H. C.: Light Scattering by Small Particles, Courier Dover Publications, New York, 1957. 9610

AMTD
7, 9603–9671, 2014

Sensitivity of O_2 A-band measurements to clouds

S. Sanghavi et al.

Van Diedenhoven, B., Hasekamp, O., and Landgraf, J.: Retrieval of cloud parameters from satellite-based reflectance measurements in the ultraviolet and the oxygen A-band, J. Geophys. Res.-Atmos., 112, D15208, doi:10.1029/2006JD008155 , 2007. 9605
Wiscombe, W. J.: Improved Mie scattering algorithms, Appl. Optics, 19, 1505–1509, 1980. 9610

AMTD
7, 9603–9671, 2014

Table 1. O_2 A-band wavelengths representing column absorption strengths near $\tau_{abs,0}$ = 0, 1, 10, 20 and 30.

Wavelength [nm]	$\tau_{abs,0}$
750.00	0.0
762.95	0.995
762.53	9.755
763.85	20.030
761.26	28.216

AMTD
7, 9603–9671, 2014

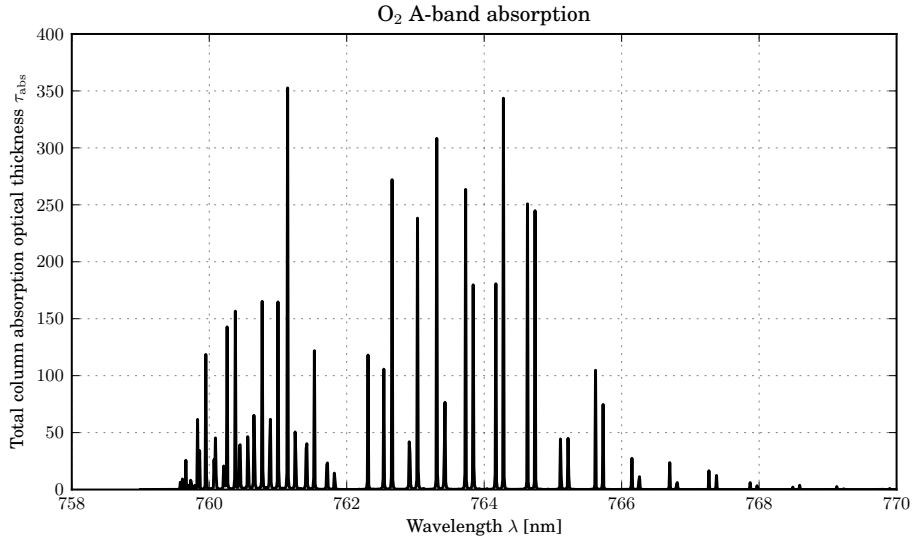

Figure 1. Absorption optical thickness due to O_2 A-band line absorption for the total column of a mid-latitude summer atmosphere.

AMTD
7, 9603–9671, 2014

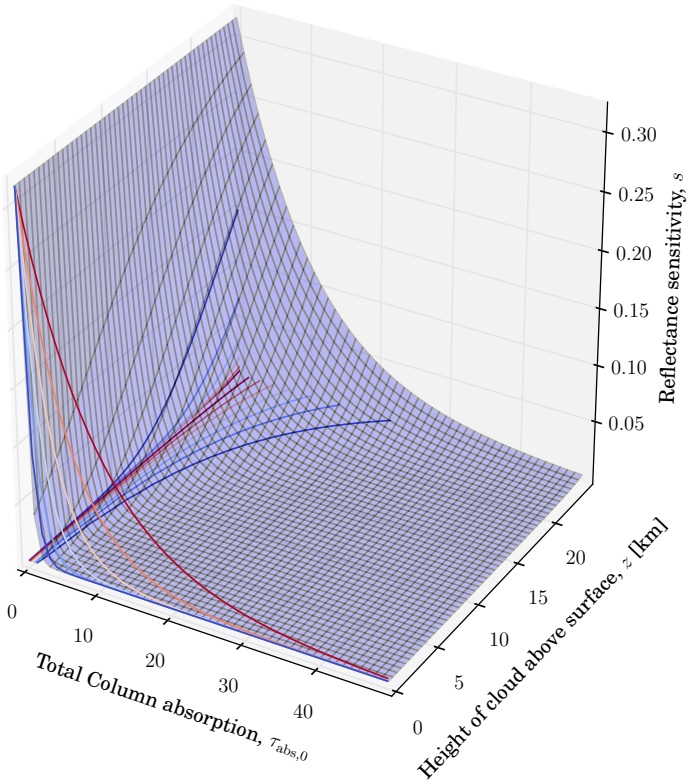

Figure 2. Sensitivity s to Lambertian laminar reflectance of albedo $\omega_0 = 1$ at height z above a black surface in a purely absorbing atmosphere ($\theta_{Sun} = \theta_{View} = 0$) as a function of total column absorption strength, $\tau_{abs,0}$ (assuming an exponential concentration profile of scale height $H = 8$ and uniform absorption cross-section at all levels).

AMTD
7, 9603–9671, 2014

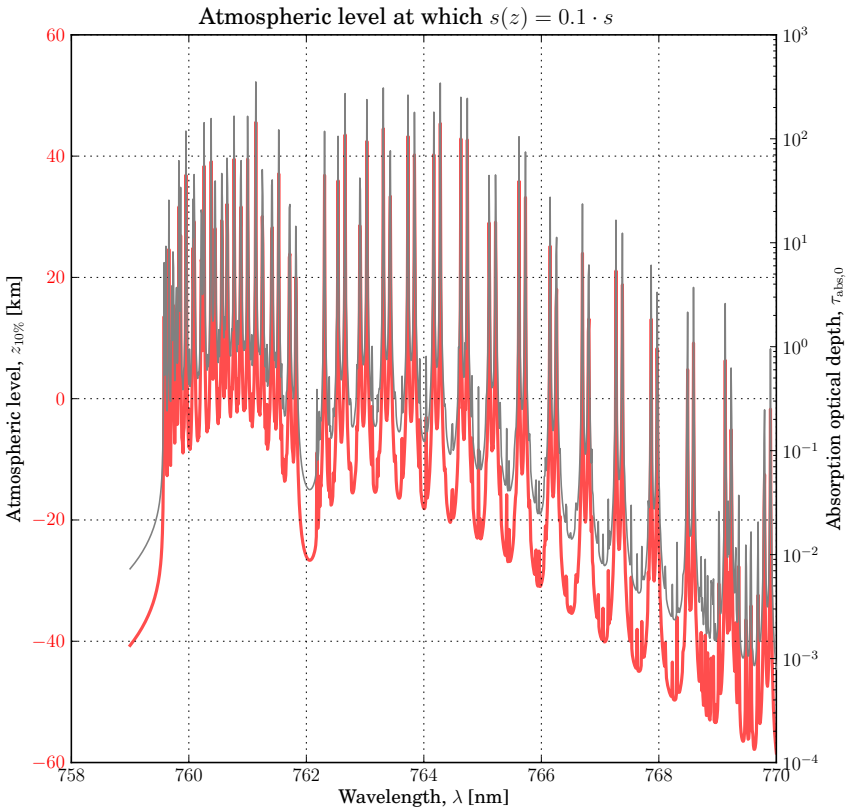

Figure 3. The atmospheric height (red) above the surface at which the sensitivity to reflectance is expected to be reduced to s = 0.03 or about 10 % of the sensitivity at the top of atmosphere (TOA). Negative heights are unphysical (below the surface) and indicate that all atmospheric levels above the surface are more sensitive than s = 0.03. This height is directly proportional to the logarithm of the total absorption optical thickness, shown in grey.

AMTD
7, 9603–9671, 2014

Sensitivity of O_2 A-band measurements to clouds

S. Sanghavi et al.

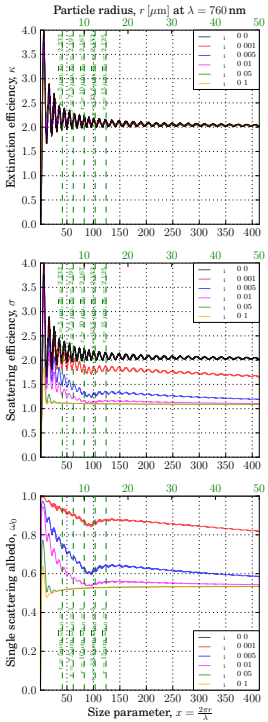

Figure 4. The dependence of the extinction, κ, (top panel) and scattering, σ, (middle panel) efficiencies and the single scattering albedo, ω_0, (bottom panel) of a single particle on size parameter, $x = \frac{2\pi r}{\lambda}$. An additional x axis on the top of each sub-figure shows the corresponding particle size at $\lambda = 760$ nm. Each panel shows values computed for water droplets ($n_r = 1.33$) but six different values of $n_i = 0, 0.001, 0.005, 0.01, 0.05$ and 0.1 as shown in each legend. Corresponding values for a lognormal size distribution of median radii $r_0 = 5, 7.5, 10, 12.5$ and $15\,\mu$m, respectively, each with a width $\sigma_0 = 1.13$ have been shown along corresponding vertical lines. Due to the narrow width of the size distribution, these size-averaged values are found to be very close to their single particle counterparts.

AMTD
7, 9603–9671, 2014

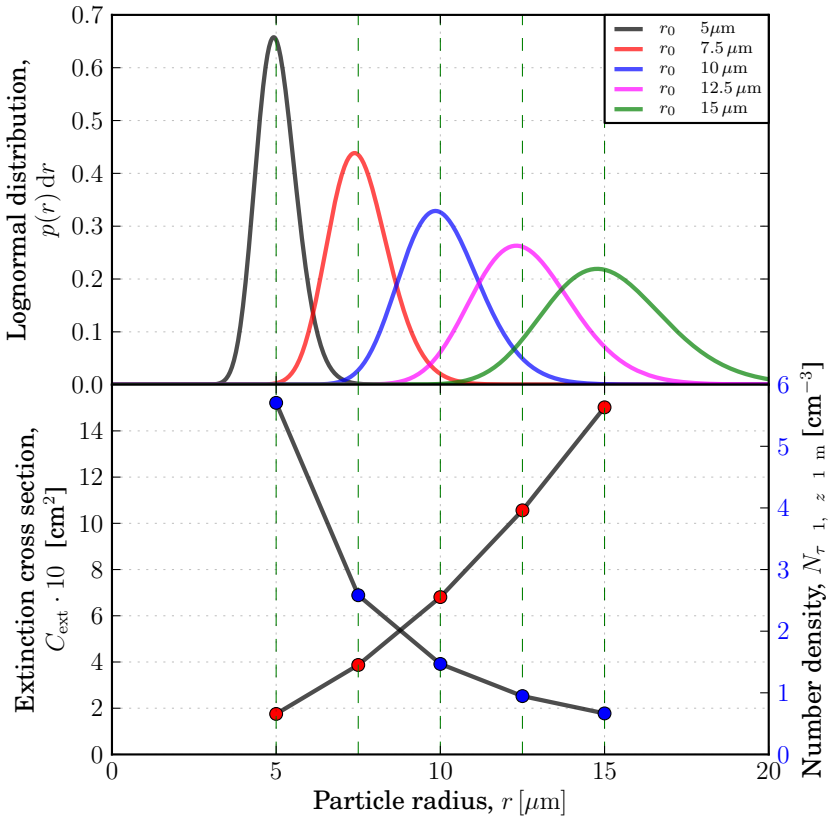

Figure 5. Top panel: log normal droplet size distributions for median radii r_0 = 5, 7.5, 10, 12.5 and 15 µm, respectively, each with a width σ_0 = 1.13. Bottom panel: extinction cross section C_{ext} [cm^2] (red) of each size distribution (left) and the corresponding number density N [droplets cm^{-3}] (blue) for a constant cloud optical thickness τ = 1 and a geometric thickness Δz = 1 km.

AMTD
7, 9603–9671, 2014

Sensitivity of O_2 A-band measurements to clouds

S. Sanghavi et al.

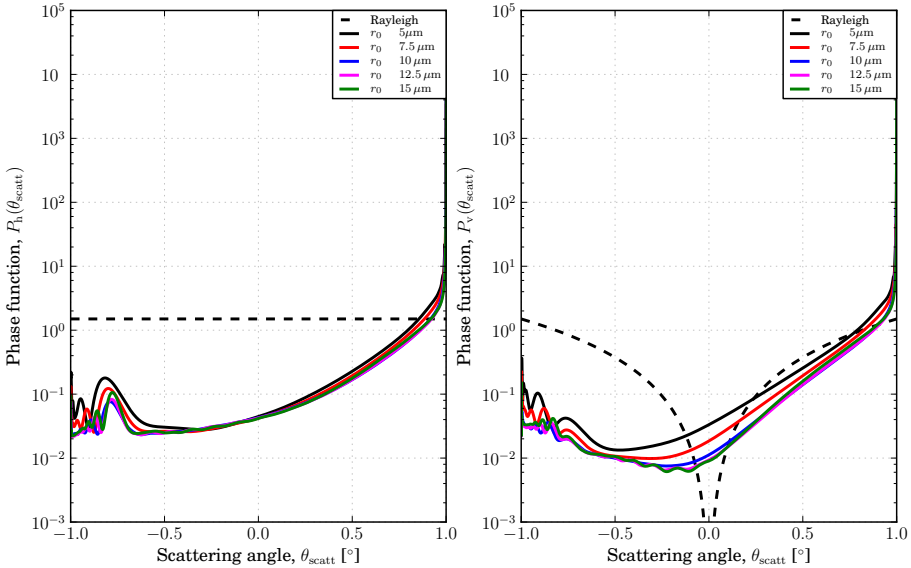

Figure 6. Phase functions $P_h(\theta_{scatt})$ and $P_v(\theta_{scatt})$ as a function of scattering angle θ_{scatt} for distributions for median radii $r_0 = 5, 7.5, 10, 12.5$ and 15 µm, respectively, each with a width $\sigma_0 = 1.13$. The refractive index in each case is $n = 1.33 - 0.0i$. The dashed line shows the corresponding Rayleigh scattering phase functions.

AMTD
7, 9603–9671, 2014

Sensitivity of O_2 A-band measurements to clouds

S. Sanghavi et al.

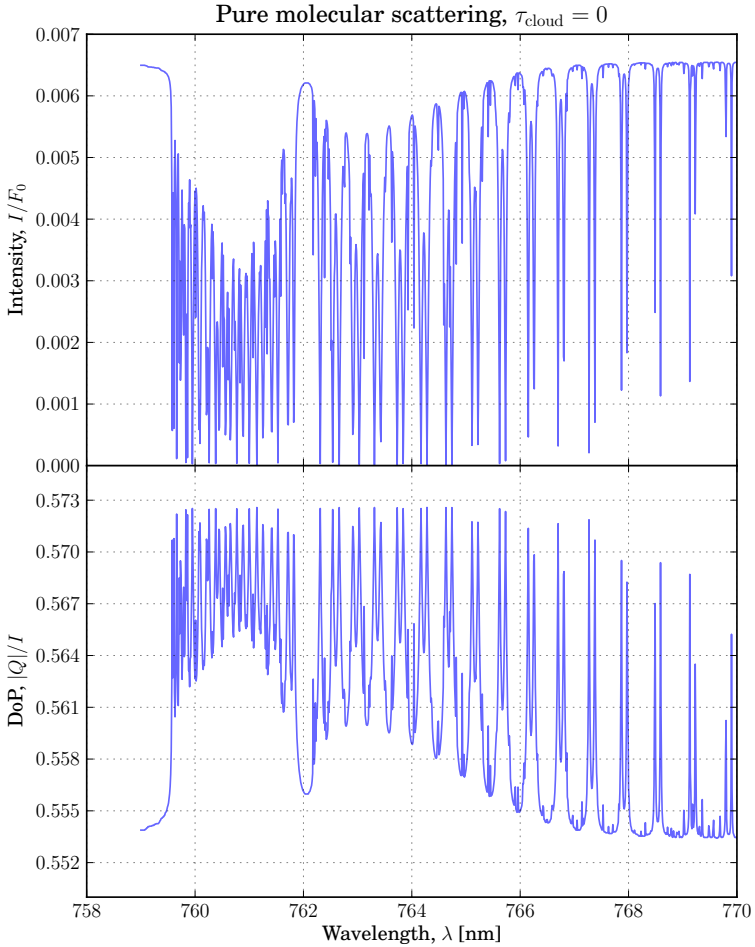

Figure 7. Intensity (top) and degree of polarization (bottom) due to Rayleigh scattering of a purely molecular atmosphere in the O_2 A-band.

AMTD
7, 9603–9671, 2014

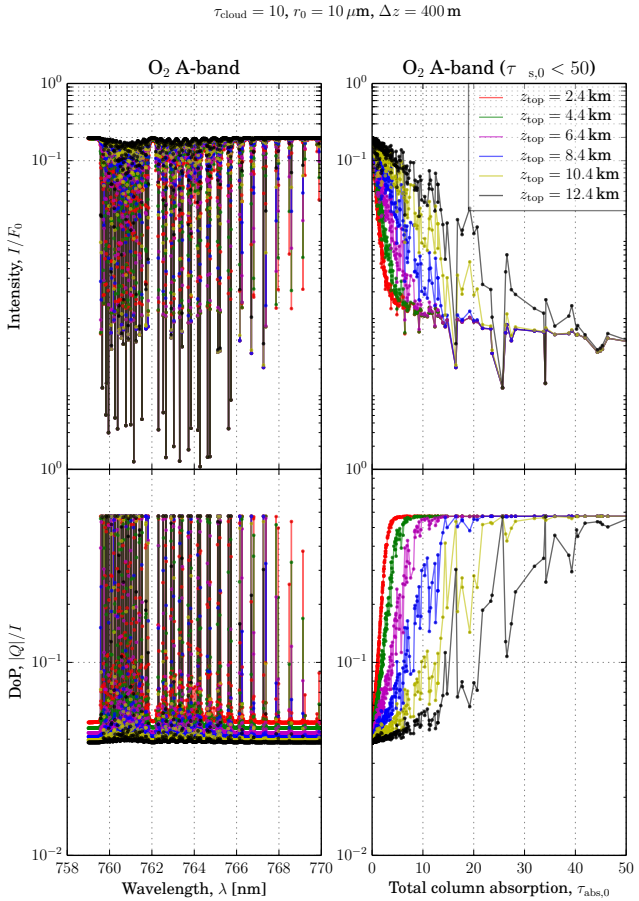

Figure 8. Intensity (top) and degree of polarization (bottom) due to a cloud-laden atmosphere of constant cloud optical depth, $\tau_{\text{cloud}} = 10$, with median droplet radius $r_0 = 10\,\mu\text{m}$ but varying cloud top heights z_{top} (but constant geometric thickness $\Delta z = 400\,\text{m}$) in the O_2 A-band.

AMTD
7, 9603–9671, 2014

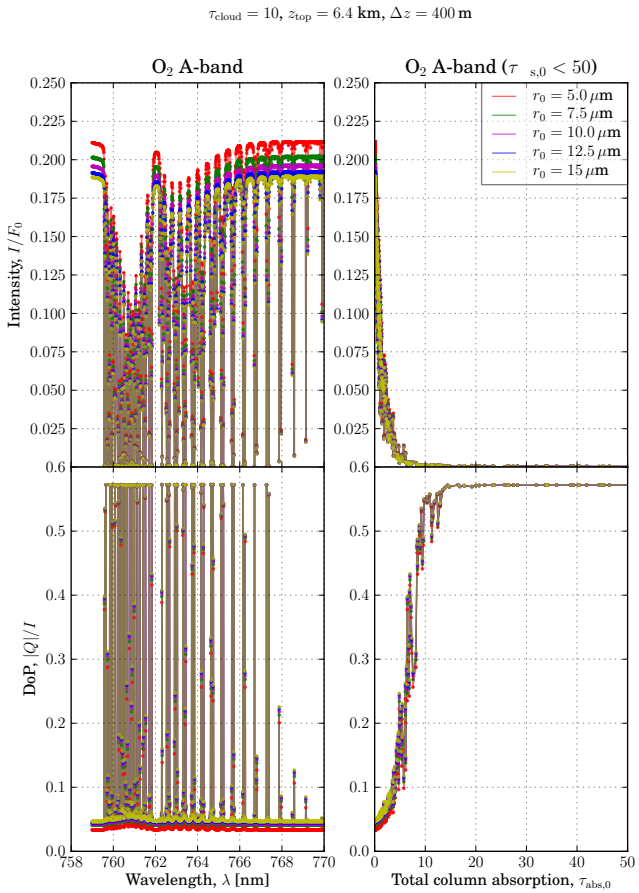

Figure 9. Intensity (top) and degree of polarization (bottom) due to a cloud-laden atmosphere of constant cloud optical depth, $\tau_{\text{cloud}} = 10$ at a top height of $z_{\text{top}} = 6.4$ km but varying median cloud droplet radii in the O_2 A-band.

AMTD
7, 9603–9671, 2014

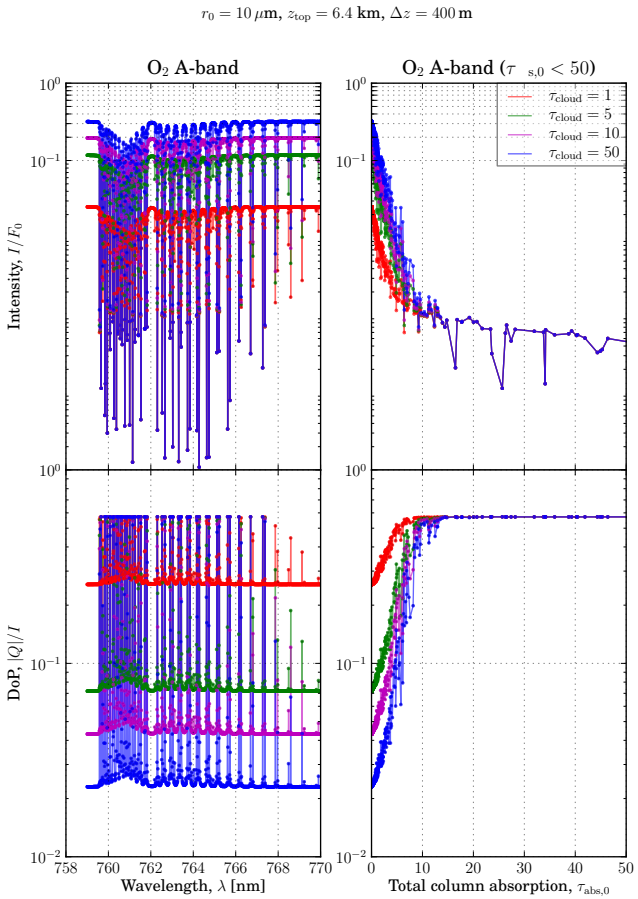

Figure 10. Intensity (top) and degree of polarization (bottom) due to a cloud-laden atmosphere of constant cloud droplet size, r_0 = 10 µm, at a top height of z_{top} = 10.4 km but varying cloud optical thickness τ_{cloud} in the O$_2$ A-band.

AMTD
7, 9603–9671, 2014

Sensitivity of O$_2$ A-band measurements to clouds

S. Sanghavi et al.

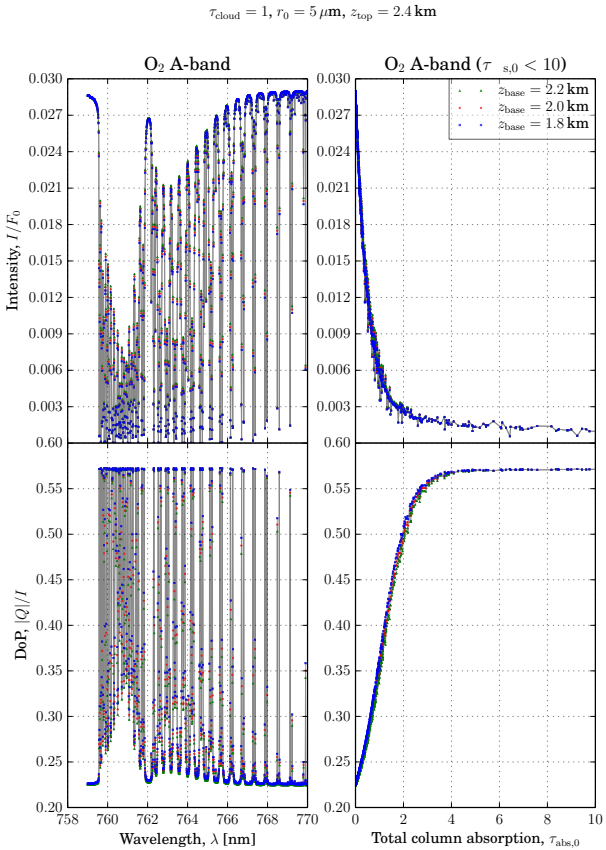

Figure 11. Intensity (top) and degree of polarization (bottom) plotted against wavelength (left) and column absorption strength, $\tau_{\text{abs},0}$ (right) due to a cloud-laden atmosphere of constant cloud optical depth, $\tau_{\text{cloud}} = 1$, median droplet radius $r_0 = 5\,\mu\text{m}$, cloud top height $z_{\text{top}} = 2.4\,\text{km}$ but varying cloud geometric heights $\Delta z = 200\,\text{m}$ (blue), $\Delta z = 400\,\text{m}$ (red) and $\Delta z = 600\,\text{m}$ (green).

AMTD
7, 9603–9671, 2014

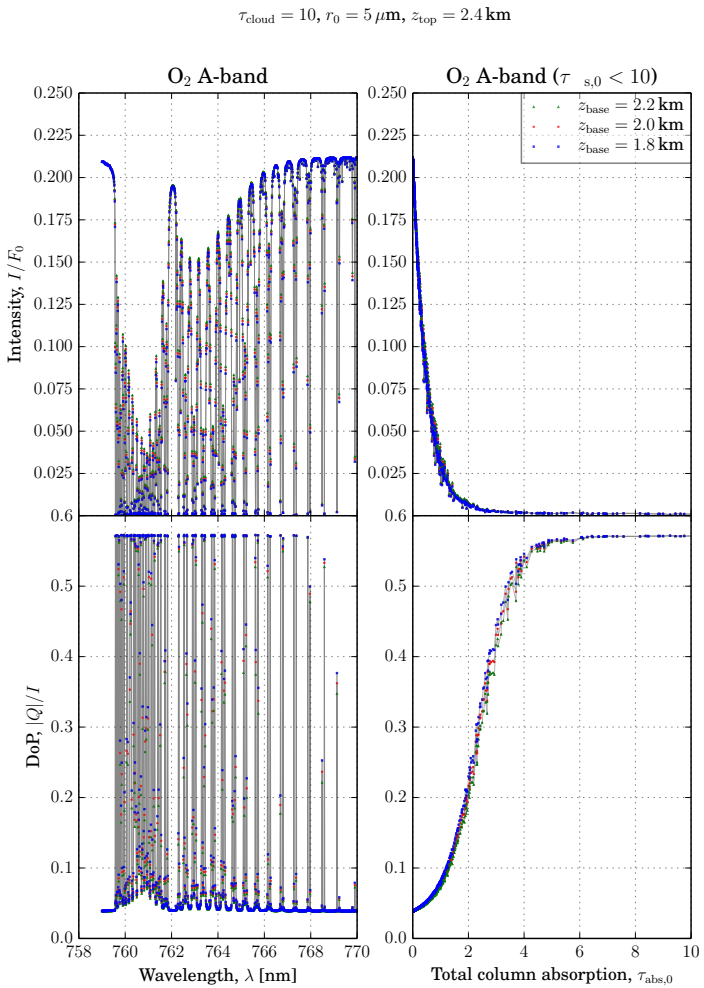

Figure 12. Same as Fig. 11 except for a thick cloud of optical thickness τ_{cloud} = 10.

AMTD
7, 9603–9671, 2014

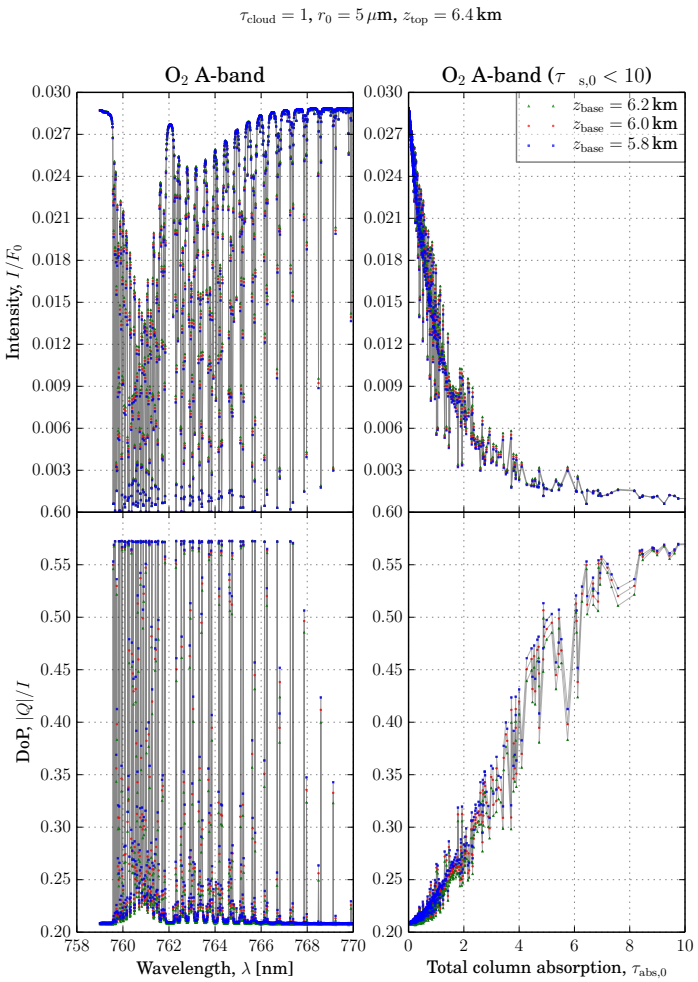

Figure 13. Same as Fig. 11 except for a cloud top height of z_{top} = 6 km.

AMTD
7, 9603–9671, 2014

Sensitivity of O_2 A-band measurements to clouds

S. Sanghavi et al.

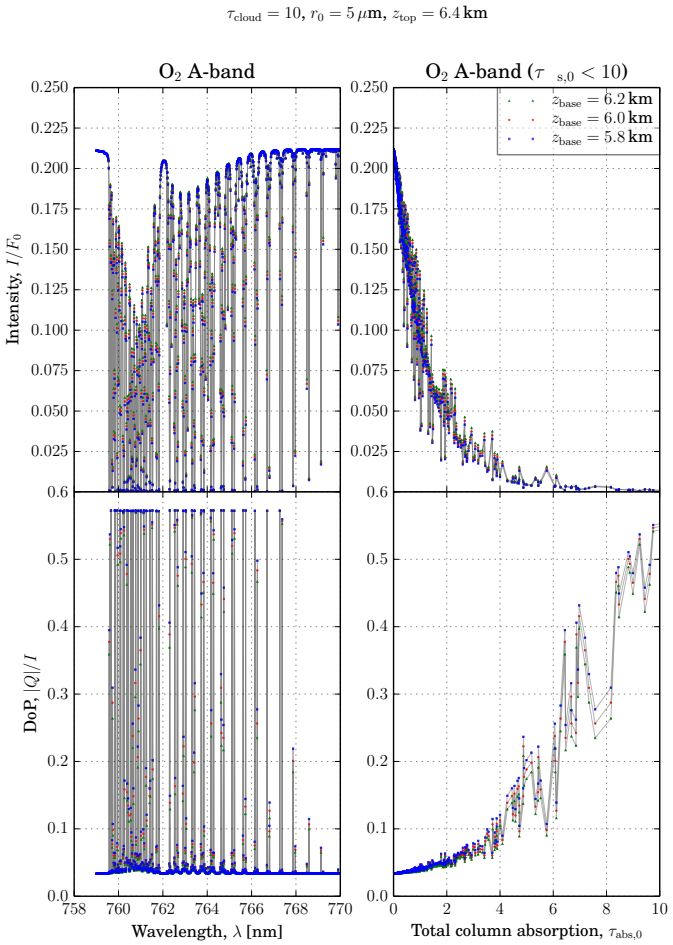

Figure 14. Same as Fig. 11 except for a thick cloud of optical thickness $\tau_{\mathrm{cloud}} = 10$ at a top height of $z_{\mathrm{top}} = 6$ km.

AMTD
7, 9603–9671, 2014

Sensitivity of O$_2$ A-band measurements to clouds

S. Sanghavi et al.

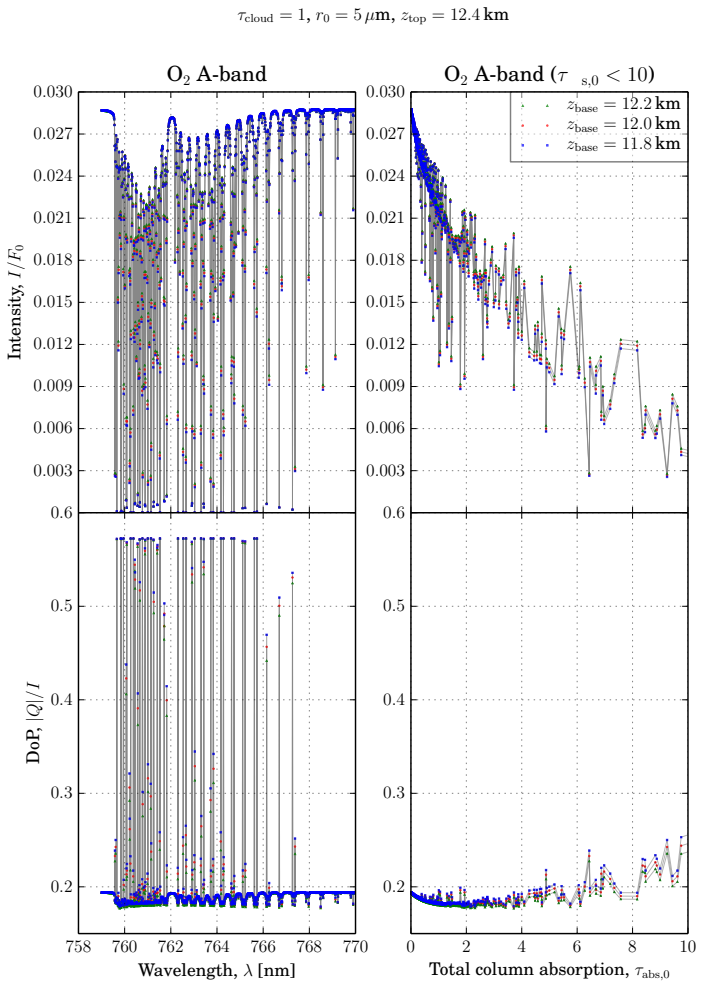

Figure 15. Same as Fig. 11 except for a cloud top height of z_{top} = 12 km.

AMTD
7, 9603–9671, 2014

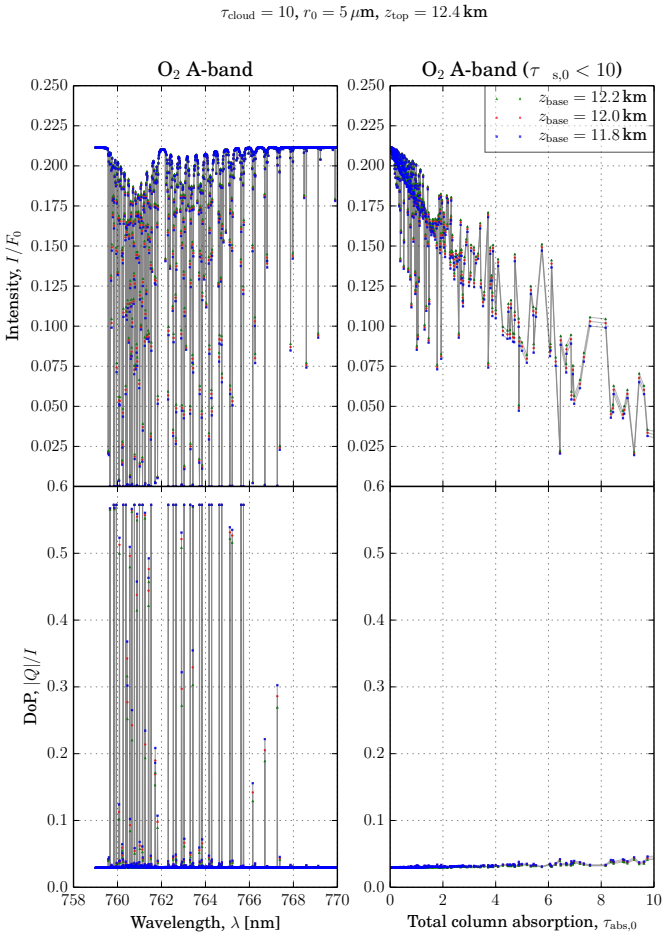

Figure 16. Same as Fig. 11 except for a thick cloud of optical thickness $\tau_{\text{cloud}} = 10$ at a top height of $z_{\text{top}} = 12\,\text{km}$.

AMTD
7, 9603–9671, 2014

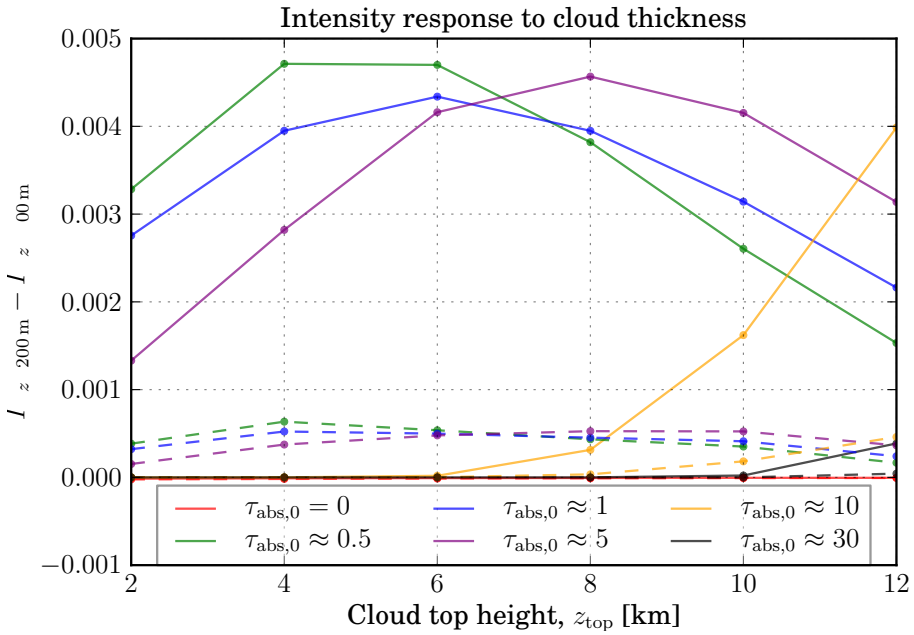

Figure 17. Height dependence of the change in intensity due to a change in cloud thickness from Δz = 200 m to Δz = 600 m for different total column absorption strengths (represented by different line colors). The solid lines represent a thick cloud of optical depth, τ_{cloud} = 10 while broken lines show a thin cloud of optical depth, τ_{cloud} = 1.

AMTD
7, 9603–9671, 2014

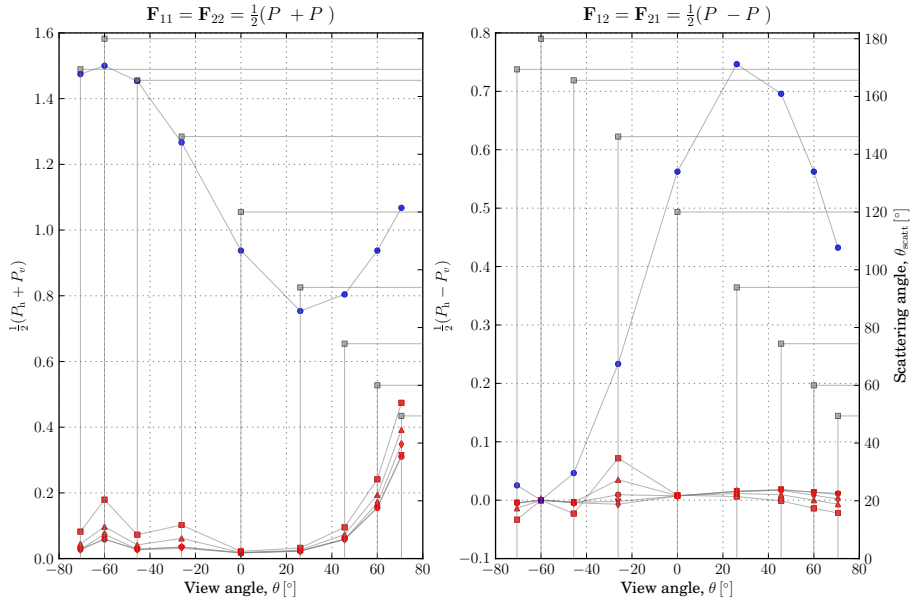

Figure 18. Elements F_{11} (left panel) and F_{21} (right panel) of the scattering matrix $\mathbf{F}(\theta_{\mathrm{scatt}})$ for Rayleigh scattering (blue circles) as well as due to different cloud droplet sizes shown in red using different marker shapes (a square for $r_0 = 5\,\mu\mathrm{m}$, a triangle pointing up for $r_0 = 7.5\,\mu\mathrm{m}$, a circle for $r_0 = 10\,\mu\mathrm{m}$, a triangle pointing down for $r_0 = 12.5\,\mu\mathrm{m}$ and a diamond for $r_0 = 15\,\mu\mathrm{m}$). Given a solar zenith angle $\theta_0 = 60^\circ$, the scattering angle θ_{scatt} is shown on the right oordinate of each panel (grey squares) as a function of view angle within the principal plane.

AMTD
7, 9603–9671, 2014

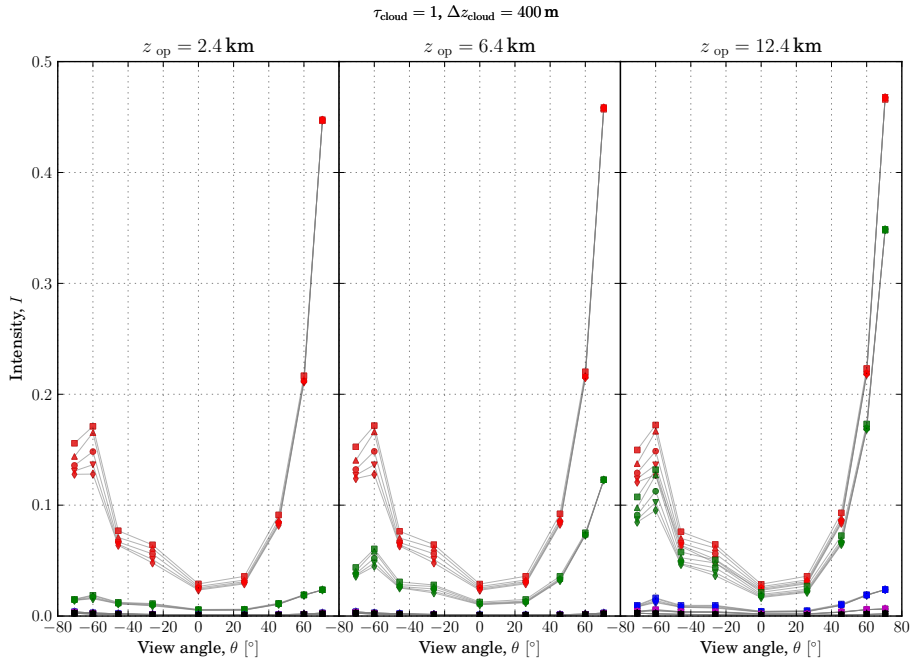

Figure 19. Simulated intensities *I* with respect to view angle θ_{view} for clouds of optical thickness $\tau_{\text{cloud}} = 1$ and of varying droplet size $r_0 \in \{5, 7.5, 10, 12.5, 15\}$ µm at wavelengths of different column absorption strengths $\tau_{\text{abs},0} \in \{0, 1, 10, 20, 30\}$, respectively. The three panels represent cloud top heights of $z_{\text{top}} = 2.4$, 6.4 and 12.4 km, respectively.
Markers of different shapes have been used to represent different droplets sizes: a square is used for $r_0 = 5$ µm, a triangle pointing up for $r_0 = 7.5$ µm, a circle for $r_0 = 10$ µm, a triangle pointing down for $r_0 = 12.5$ µm and a diamond for $r_0 = 15$ µm.
Colors have been used for different column absorption strengths: red for $\tau_{\text{abs},0} = 0$, green for $\tau_{\text{abs},0} = 1$, blue for $\tau_{\text{abs},0} = 10$, magenta for $\tau_{\text{abs},0} = 20$ and black for $\tau_{\text{abs},0} = 30$.

AMTD
7, 9603–9671, 2014

Sensitivity of O_2 A-band measurements to clouds

S. Sanghavi et al.

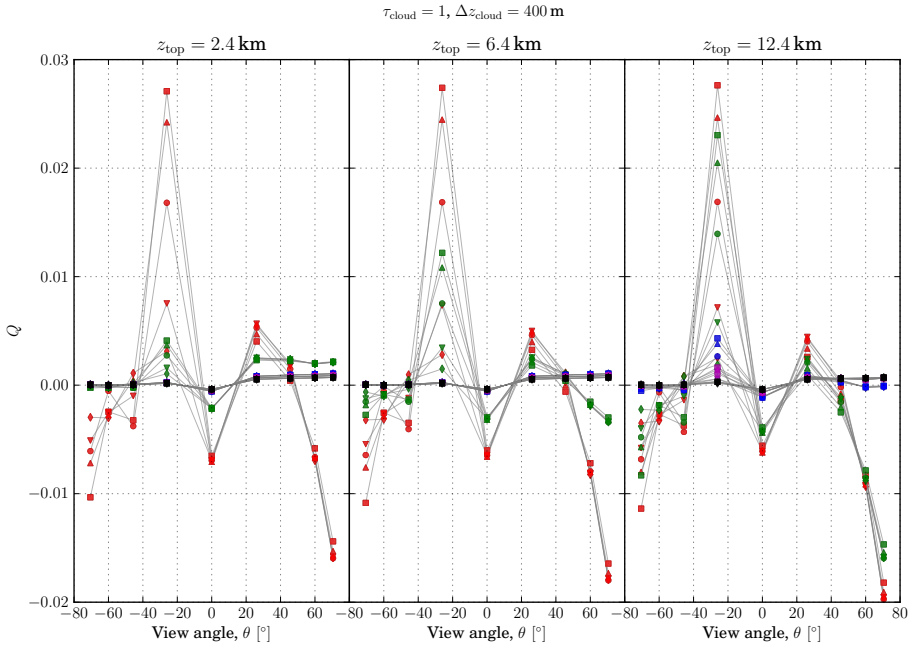

Figure 20. Same as Fig. 19 except that the Stokes component *Q* is shown instead of *I*.

AMTD
7, 9603–9671, 2014

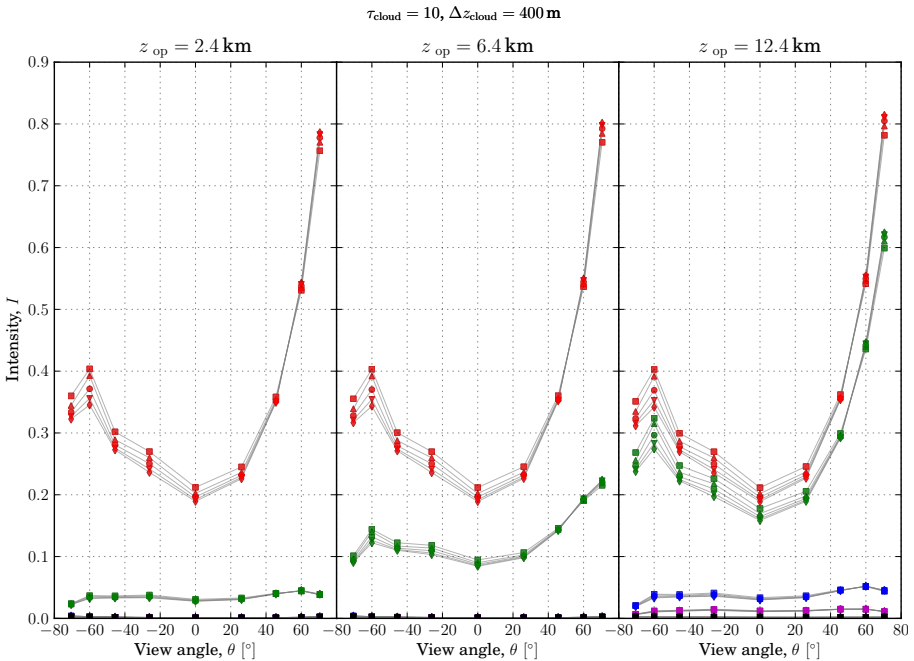

Figure 21. Same as Fig. 19 except that the Stokes component *I* is shown for a cloud of optical thickness τ_{cloud} = 10.

AMTD
7, 9603–9671, 2014

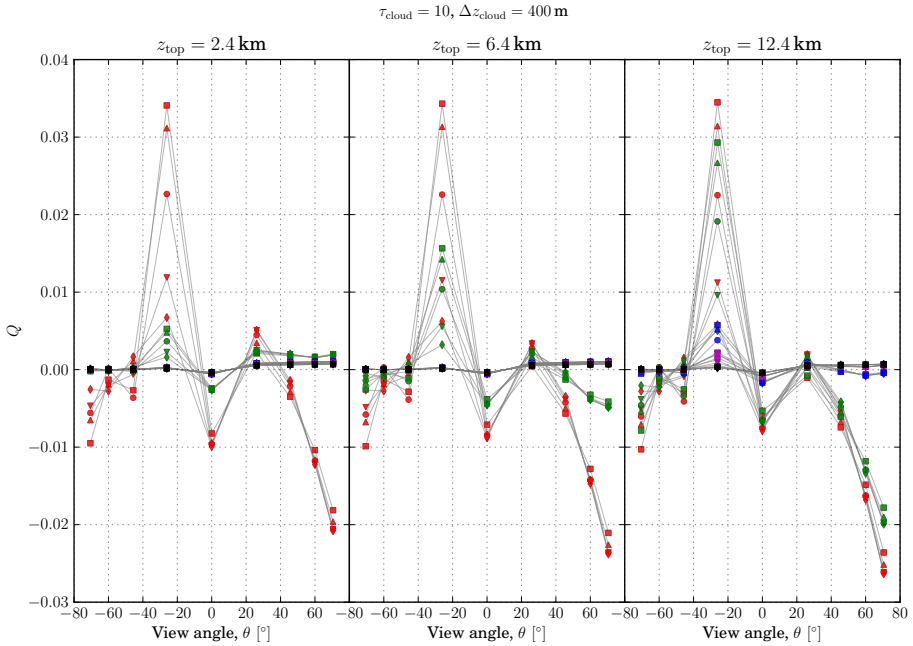

Figure 22. Same as Fig. 21 except that the Stokes component *Q* is shown instead of *I*.

AMTD
7, 9603–9671, 2014

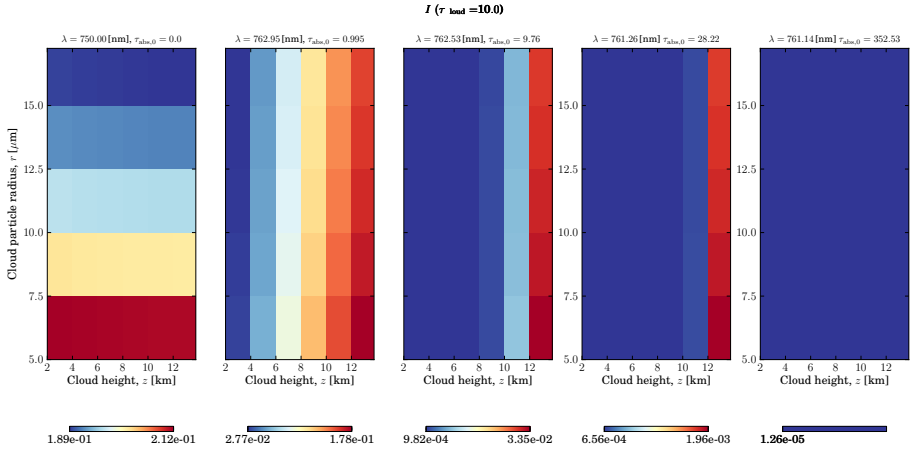

Figure 23. I at $\tau_{\text{cloud}} = 10$.

AMTD
7, 9603–9671, 2014

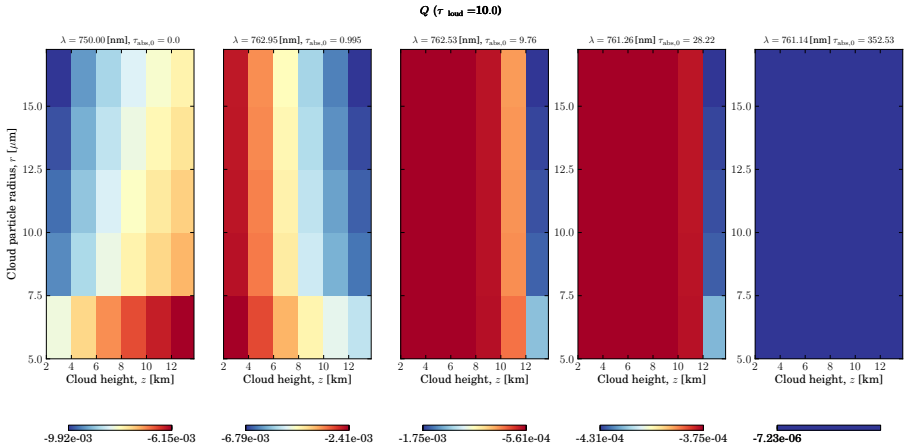

Figure 24. Q at $\tau_{\text{cloud}} = 10$.

AMTD
7, 9603–9671, 2014

Sensitivity of O_2 A-band measurements to clouds

S. Sanghavi et al.

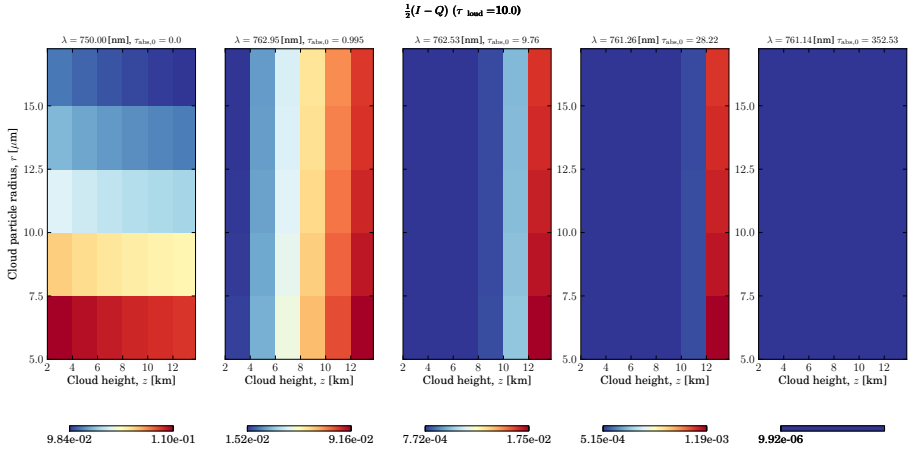

Figure 25. $I - Q$ at $\tau_{\text{cloud}} = 10$.

AMTD
7, 9603–9671, 2014

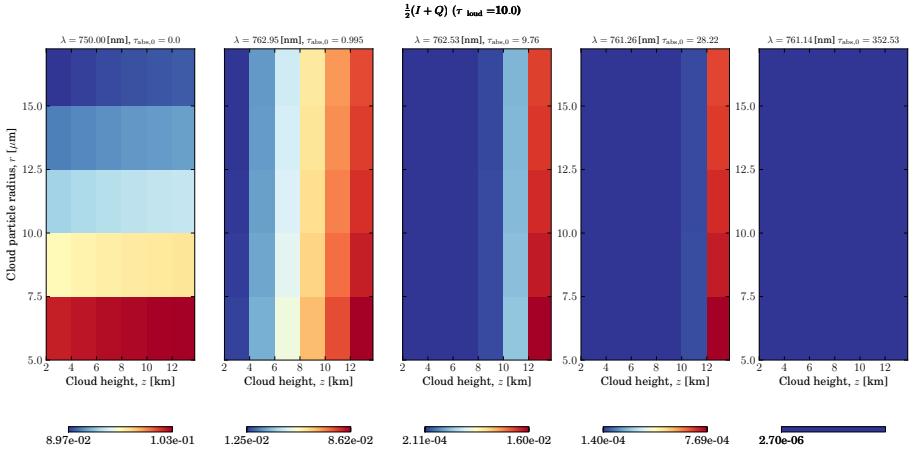

Figure 26. $I + Q$ at $\tau_{\text{cloud}} = 10$.

AMTD
7, 9603–9671, 2014

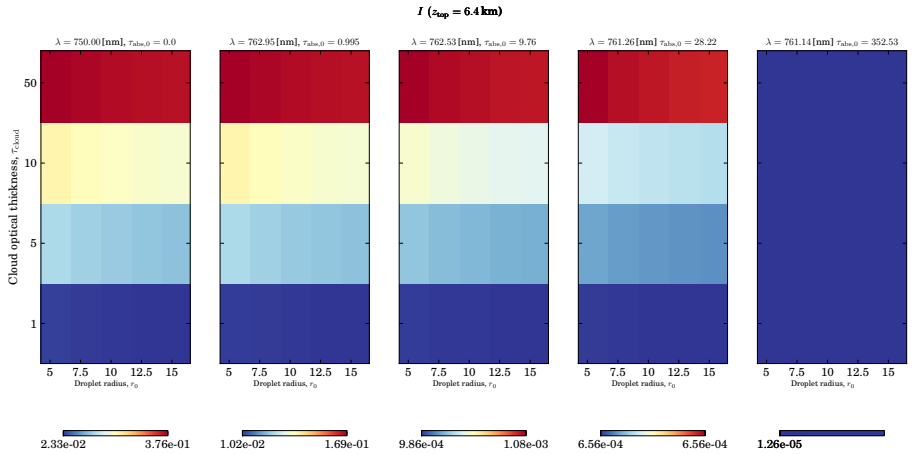

Figure 27. I at z_{top} = 6.4 km.

AMTD
7, 9603–9671, 2014

Sensitivity of O_2 A-band measurements to clouds

S. Sanghavi et al.

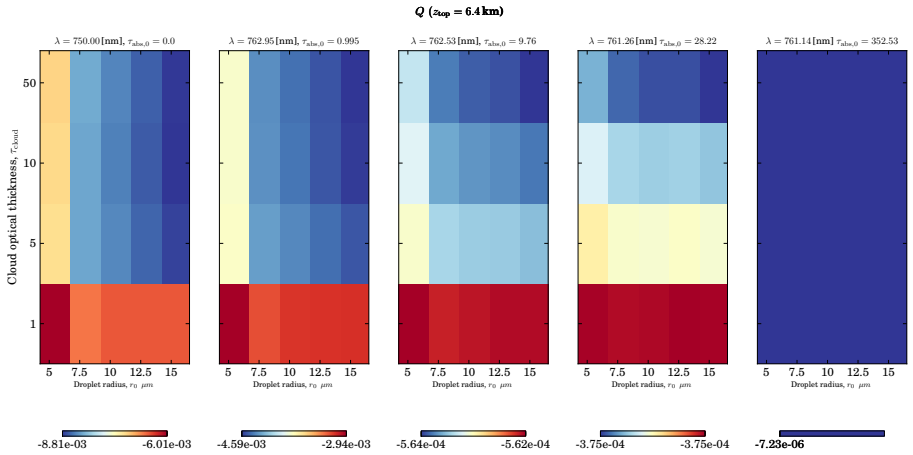

Figure 28. Q at z_{top} = 6.4 km.

AMTD
7, 9603–9671, 2014

Sensitivity of O_2 A-band measurements to clouds

S. Sanghavi et al.

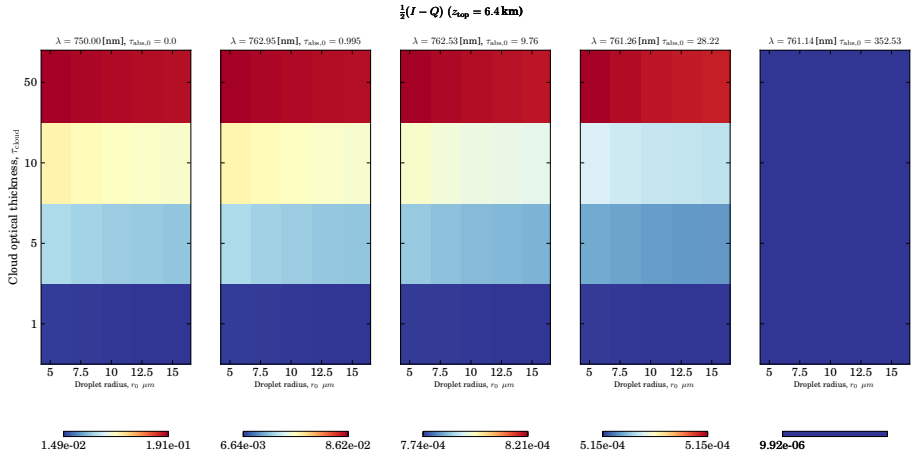

Figure 29. $I - Q$ at z_{top} = 6.4 km.

AMTD
7, 9603–9671, 2014

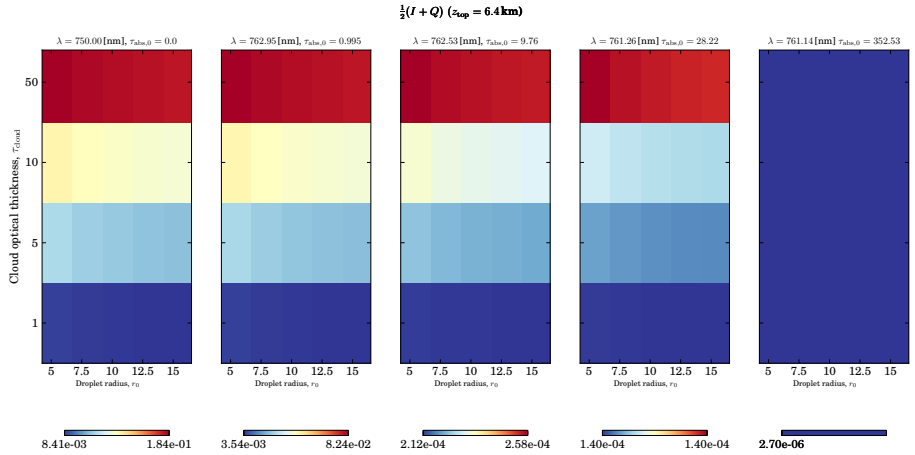

Figure 30. $I + Q$ at z_{top} = 6.4 km.

AMTD
7, 9603–9671, 2014

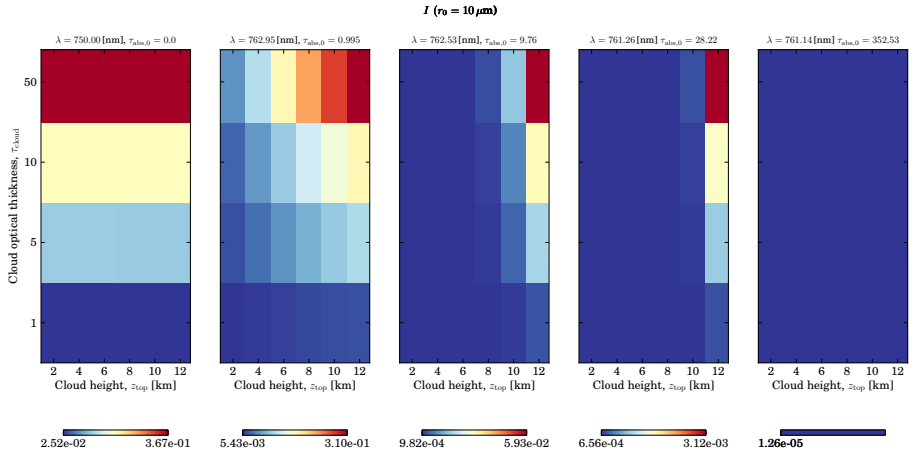

Figure 31. / at τ_{cloud} = 10.

AMTD
7, 9603–9671, 2014

Sensitivity of O_2 A-band measurements to clouds

S. Sanghavi et al.

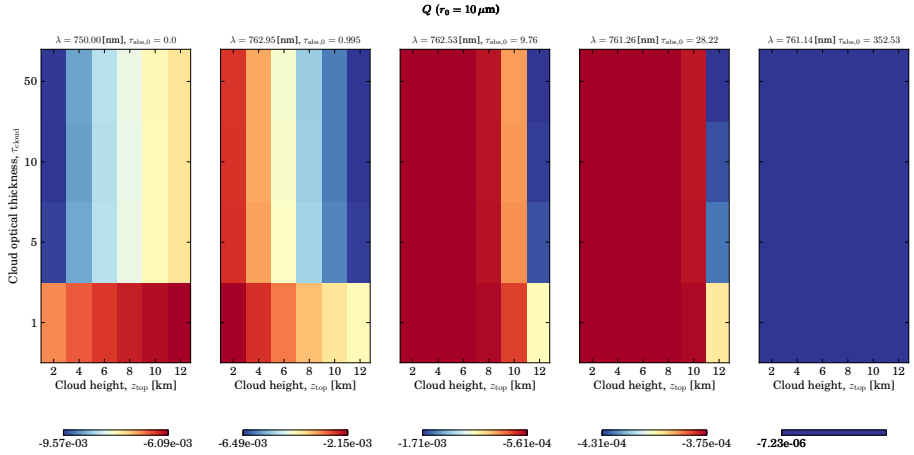

Figure 32. Q at $\tau_{cloud} = 10$.

AMTD
7, 9603–9671, 2014

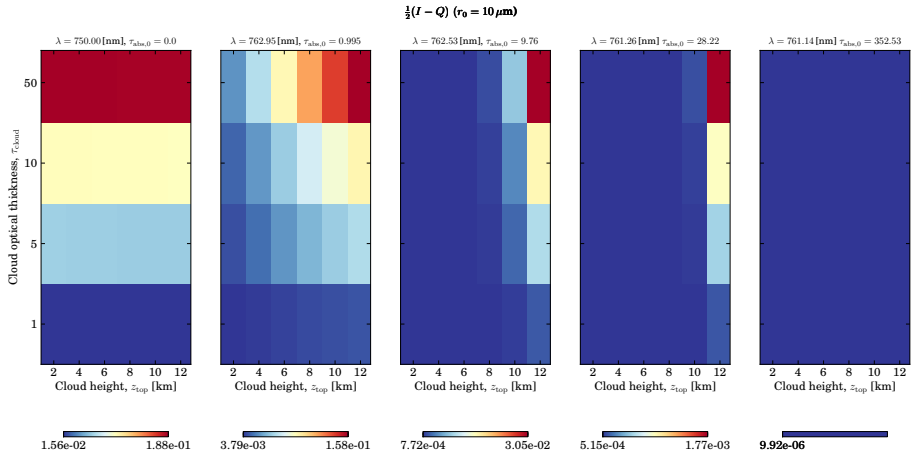

Figure 33. $I - Q$ at $\tau_{cloud} = 10$.

AMTD
7, 9603–9671, 2014

Sensitivity of O_2 A-band measurements to clouds

S. Sanghavi et al.

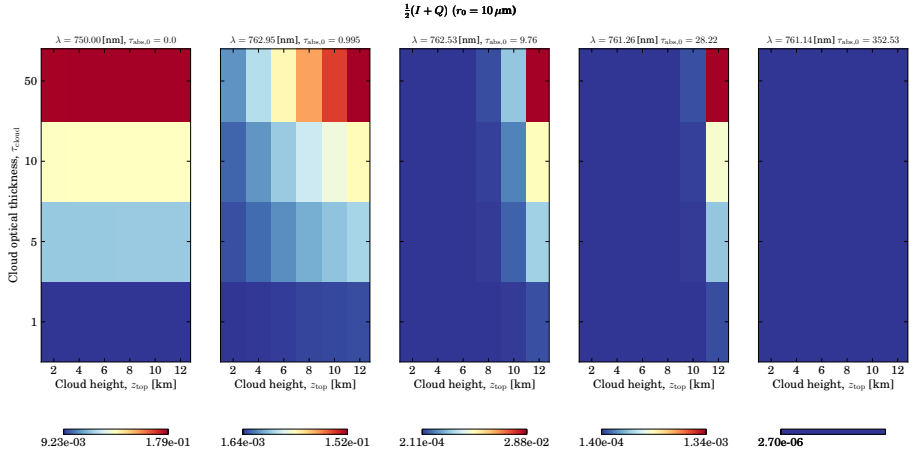

Figure 34. $I + Q$ at $\tau_{cloud} = 10$.

AMTD
7, 9603–9671, 2014